PHYSICAL REVIEW C **110**, 015803 (2024)

(p, γ) cross section measurements on Sn isotopes relevant to the p process

S. Harissopulos,[*] E. Vagena, A. Spyrou,[†] M. Axiotis, Z. Kotsina, K. Tsampa, and A. Lagoyannis
Tandem Accelerator Laboratory, Institute of Nuclear and Particle Physics, NCSR "Demokritos", 153.10 Aghia Paraskevi, Athens, Greece

P. Dimitriou
Nuclear Data Section, International Atomic Energy Agency, Vienna 1400, Austria

H.-W. Becker and V. Foteinou
DTL/RUBION, Ruhr-Universität Bochum, 40781 Bochum, Germany

(Received 4 November 2023; revised 10 March 2024; accepted 21 June 2024; published 16 July 2024)

Background: Calculations of p-nuclei abundances depend heavily on the Hauser-Feshbach (HF) theory to compute cross sections and, consequently, the reaction rates entering a huge reaction network encompassing nearly 2000 isotopes, the vast majority of which are unstable. Therefore, the successful reproduction of p-nuclei abundances relies on the reliability of the nuclear parameters entering the HF calculations, i.e., the optical model potential (OMP), the nuclear level density (NLD), and the γ-ray strength function (γSF).
Purpose: New cross sections, astrophysical S factors, and reaction rates for (p, γ) reactions on ^{116}Sn and ^{118}Sn were measured at energies relevant to the p process with the aim of validating OMP, NLD, and γSF models and investigating their "global" character, with particular emphasis on the Lane-consistent semimicroscopic OMP developed by Bauge *et al.* [Bauge, Delaroche, and Girod, Phys. Rev. C **63**, 024607 (2001)].
Method: Cross sections were determined from γ-angular distribution measurements, angle-integrated γ spectra taken with the 4π γ-summing technique, and off-beam γ activities measured with the activation method. HF calculations were performed with the TALYS code (version 1.96).
Results: Total and partial cross sections were determined for the ^{116}Sn$(p, \gamma)^{117}$Sb and ^{118}Sn$(p, \gamma)^{119}$Sb reactions at energies ranging from 2.2 to 5.2 MeV. These energies cover almost entirely the Gamow window relevant to p-process nucleosynthesis. The experimentally determined cross sections and the resulting S factors were corrected for electron screening effects and subsequently compared with HF calculations, which were performed using various combinations of phenomenological or semi-microscopic models describing the proton-nucleus OMP (p-OMP), alpha-particle–nucleus OMP (α-OMP), NLD, and γSF.
Conclusions: Our screening-corrected data were found to be in very good agreement with the corresponding calculations performed using a combination of the p-OMP of Bauge *et al.* with semimicroscopic models for the α-OMP, NLD, and γSF. This agreement resulted from adjusting the energy dependent isoscalar normalization factors λ_V and λ_W for the real and imaginary components of the OMP. The model combination used by default in TALYS 1.96, which includes only phenomenological models for the nuclear parameters entering the HF calculations, was less successful in reproducing our screening-corrected data. The NLDs used in our TALYS calculations were compared with the experimental cumulative numbers of low-lying levels observed in ^{117}Sb and ^{119}Sb. Average radiative widths from the systematics were also used to validate the combination of NLD and γSF models found to best reproduce our data. Finally, the stellar reaction rates obtained in the present work were compared with those provided in the REACLIB and BRUSLIB databases. In the temperature range relevant to the p process, it was found that the REACLIB stellar rates are smaller by a factor of ≈2, whereas the BRUSLIB rates exhibit deviations of no more than 20%.

DOI: 10.1103/PhysRevC.110.015803

I. INTRODUCTION

The vast majority of the (p, γ) cross-section measurements carried out in the last two decades on nuclei heavier than iron have been motivated by the need to perform a credibility test of the statistical model calculations that are based on the Hauser-Feshbach theory [1]. These calculations are required to provide the cross sections and, hence, the reaction rates of more than 20000 nuclear reactions entering a huge reaction network involving almost 2000 stable or unstable isotopes lying between Ge and Bi (see, e.g., Fig. 4 of Ref. [2]).

Solving this network is necessary to calculate the abundances of a certain group of 35 proton-rich isotopes lying

---

[*] Contact author: sharisop@inp.demokritos.gr

[†] Present address: Department of Physics and Astronomy, and Facility for Rare Isotope Beams, Michigan State University, East Lansing, Michigan 48824, USA.

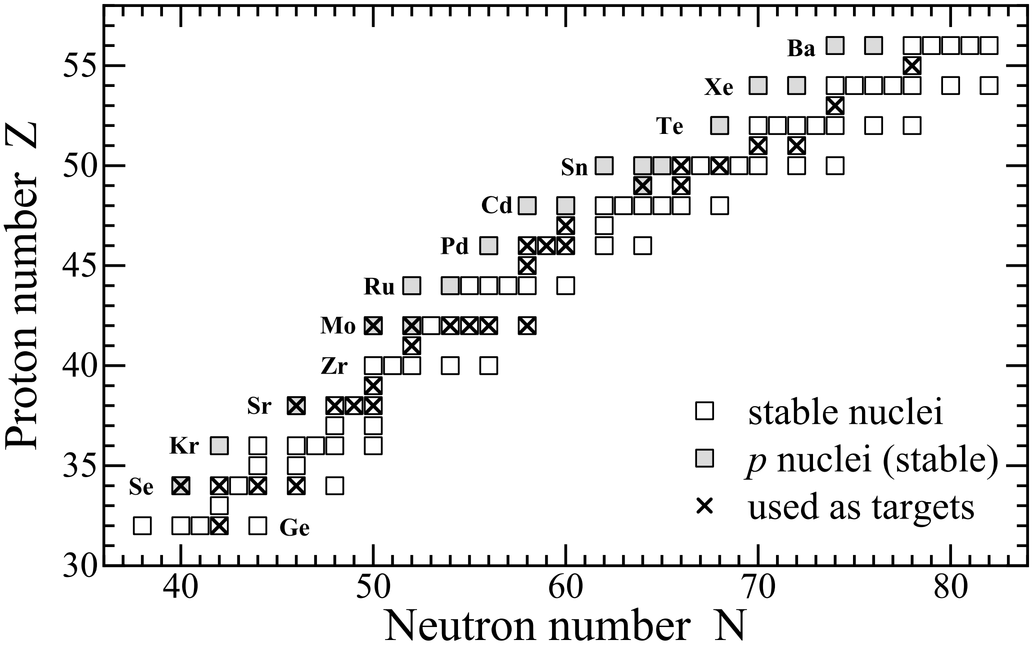

FIG. 1. Map of the stable nuclides (boxes) between Ge and Ba. Gray boxes indicate *p* nuclei. Nuclides marked with an "X" indicate the isotopes used as targets in (p,γ) cross-section measurements reported in Refs. [2,8–22].

between ^{74}Se and ^{196}Hg, known as *p* nuclei [3]. As the vast majority of the isotopes entering this network are unstable and, therefore, experimentally difficult to reach, the network's solution relies almost entirely on the predictions of the Hauser-Feshbach (HF) theory [1].

Under these conditions, uncertainties in the *p*-nuclei abundance calculations may result not only from deficiencies in the astrophysical models aimed at describing the nucleosynthetic process of the *p* nuclei in the cosmos, known as the *p* process [3–5], but also from uncertainties in the key nuclear properties used in HF calculations. These properties notably include the nucleon–nucleus and α-particle–nucleus optical model potentials (OMPs), nuclear level densities (NLDs) and γ-ray strength functions (γSFs).

p nuclei are believed to be produced in explosive stellar sites [3] under specific temperature conditions, isotopic composition, explosion mechanisms, and timescales. The choice of these parameters, the application of physical principles, and their theoretical treatment define the level of success of various *p*-process models in reproducing the observed *p*-nuclei abundances in the solar system. To achieve this task, various astrophysical scenarios and mathematical approaches have been proposed, some of which claim to be capable of reproducing the majority of these abundances with uncertainties smaller than a factor of 3 for essentially all *p* isotopes (see, e.g., [6,7]).

As some of the astrophysical conditions assumed to model the nucleosynthesis of the *p* isotopes are under debate, it is imperative to independently investigate potential uncertainties in the key nuclear properties used in the HF calculations, such as OMPs, NLDs, and γSFs. This task requires extensive comparisons between theoretical predictions and experimental data over the mass range where the *p*-process reaction network operates, i.e., from $A \approx 60$ to $A \approx 180$.

Motivated by these challenges and as a continuation of our previous communications, we present here our latest work within a series of 30 (p,γ) reaction cross-section measurements conducted by our group or in collaboration with other research teams, in the mass region $A = 74$ to 131 at energies ranging from ≈1.5 to 5 MeV. The stable nuclides used as targets in these experiments are displayed in Fig. 1.

In this paper, we report on (p,γ) cross-section measurements on Sn isotopes. Similarly to our most recent publications [19–22], this paper focuses on testing the global character of existing microscopic models for the proton-nucleus OMPs (*p*-OMPs), NLDs, and γSFs.

II. SETUPS AND MEASUREMENTS

The cross sections reported in the present work were determined using three different methods: measuring γ-angular distributions, angle-integrated γ rays with the 4π γ-summing technique, and off-beam γ activities with the activation method. Detailed descriptions of all three methods and the corresponding setups used in this work can be found in [2]. The corresponding experiments were conducted at the following facilities: the 4 MV single-stage Dynamitron accelerator at the former Institut für Strahlenphysik (now closed) of the University of Stuttgart, Germany; the 4 MV Dynamitron Tandem accelerator at Ruhr-Universität Bochum, Germany; and the 5.5 MV Tandem accelerator at NCSR "Demokritos," Athens, Greece.

Table I summarizes the energy range covered by the present work and the properties of the Sn targets used. As listed in this table, both natural and enriched targets were employed. The enriched targets were prepared by evaporating highly enriched isotopic material onto 0.2-mm-thick tantalum disks. The areal densities ξ of the targets, often referred

TABLE I. Nuclear reactions investigated in the present work. The method applied is given in the second column. The incident beam energies E_p covered and typical proton-beam currents i_p on target are given in the third and fourth columns, respectively. The uncertainty in E_p is $\leqslant$5 keV. The material used to prepare the targets via evaporation on tantalum backings is indicated in the fifth column, whereas the radial density ("thickness") ξ of the corresponding target isotope and its enrichment are given in the sixth and seventh columns, respectively. In the case of ^{116}Sn O$_2$, the ξ values refer solely to the ^{116}Sn isotope. The listed enrichments were obtained from certificates issued by the isotope-providing company. The last column gives the range of energy loss ΔE of the proton beam in the corresponding target for the minimum and maximum energies measured. This range was obtained using the code SRIM [23]. The relative uncertainty of the calculated ΔE values is less than ≈5%.

Reaction	Method	E_p (MeV)	i_p	Target material	ξ (μg/cm^2)	Enrichment (%)	ΔE (keV)
^{118}Sn$(p,\gamma)^{119}$Sb	γ-angular distributions	2.2–3.5	8–16 μA	^{118}Sn (metallic)	168±20	97.06	9.8–7.5
^{118}Sn$(p,\gamma)^{119}$Sb	4π γ-summing	2.6–5.2	9–130 nA	^{118}Sn (metallic)	168±20	97.06	9.0–5.8
^{116}Sn$(p,\gamma)^{117}$Sb	γ-angular distributions	2.3–3.5	8–15 μA	^{116}Sn O$_2$	122±8	95.74	8.7–6.8
^{116}Sn$(p,\gamma)^{117}$Sb	4π γ-summing	3.6–5.2	9–40 nA	^{116}Sn O$_2$	62±6	95.74	3.3–2.5
^{116}Sn$(p,\gamma)^{117}$Sb	activation	2.3	≈1 μA	$^{\rm nat}$Sn (metallic)	281±17	14.53	16.0
^{116}Sn$(p,\gamma)^{117}$Sb	activation	2.45	≈1 μA	$^{\rm nat}$Sn (metallic)	271±17	14.53	14.9
^{116}Sn$(p,\gamma)^{117}$Sb	activation	3.5	≈1 μA	^{116}Sn O$_2$	62±6	95.74	3.4

to as the "target thicknesses," were determined both before and after the measurements using both the x-ray fluorescence (XRF) technique (see, e.g., [24]) and Rutherford backscattering (RBS) (see, e.g., [25]).

A. γ-angular distribution measurements

The γ-angular distributions were measured using four large-volume high-purity germanium (HPGe) detectors, all shielded with bismuth germanium oxide (BGO) crystals for Compton background suppression. These detectors were placed on a motor-driven table that could rotate, allowing γ-singles spectra to be measured at eight different angles relative to the beam direction. At each proton energy, additional spectra were collected at each of the eight angles with the proton beam impinging on a blank backing to check for possible yield contributions from reactions occurring in the backing material.

The target-to-detector distances ranged from 10 to 20 cm. The current of the proton beam is given in Table I. The beam spot had a diameter of ≈4 mm. Further details about the experimental setup, procedures followed during the experiments, and checks for coincidence summing effects can be found in Refs. [2,10].

Figures 2 and 3 illustrate typical γ-singles spectra of the (p,γ) reactions on ^{116}Sn and ^{118}Sn, respectively. These spectra were taken at a proton-beam energy of 3 MeV with the Ge detector placed at an angle of 90° with respect to the beam axis. In these figures, the *primary* γ transitions deexciting the *entry* state of the produced compound nuclei ^{117}Sb and ^{119}Sb are shown in panels (c) of Figs. 2 and 3. These transitions are labeled as γ_0, γ_2, and, in the case of Fig. 3, γ_3, corresponding to the primary transitions to the ground, second, and third excited states of the respective compound nuclei based on the level listing from the IAEA's Live Chart compilation [26].

It is worth noting the absence of the primaries to the corresponding first excited states, i.e., no γ_1 is observed in both of the investigated reactions. This absence is expected because the proton beam energies used are quite low, making it so that almost entirely s-wave protons have a substantial probability of being absorbed by the target nuclei. Since the target isotopes ^{116}Sn and ^{118}Sn are even-even nuclei with ground states having spin and parity $J^\pi = 0^+$, the *entry* states of the produced compound nuclei ^{117}Sb and ^{119}Sb, are expected to have $J^\pi = 1/2^+$. As a result, these *entry* states are more likely to deexcite via γ transitions to levels with small spin differences. Therefore, γ rays from the *entry* to the first excited states of ^{117}Sb and ^{119}Sb, both having $J^\pi = 7/2^+$, are less favorable compared to those transitioning to discrete levels with $J^\pi = 1/2^+$, $3/2^+$, or $5/2^+$. These levels include the second and third excited levels and the ground state, respectively.

In addition to the primary γ rays, Figs. 2 and 3 also display all the *secondary* γ transitions depopulating discrete excited levels and feeding the corresponding ground states. These transitions are labeled with numbers in both figures, indicating their energies in keV units. Some peaks marked with an asterisk (*) indicate *secondary* γ transitions feeding discrete levels other than the corresponding ground states of the produced ^{117}Sb and ^{119}Sb isotopes. Finally, the two peaks marked with a cross (+) in panels (a) of Figs. 2 and 3 indicate the $2_1^+ \rightarrow 0_1^+$ γ transitions emitted by the ^{116}Sn$(p,p'\gamma)$ and ^{118}Sn$(p,p'\gamma)$ reactions, respectively.

Figures 2 and 3 display additional peaks. The one labeled ^{137}Cs, which appears in panels (a), corresponds to the 662-keV γ transition of a ^{137}Cs radioactive source that was used as a "clock" during the measurements to check for dead time. Additionally, the spectra shown in these figures include peaks resulting from (p,p'), (p,γ), and $(p,\alpha\gamma)$ reactions on ^{23}Na, ^{27}Al, ^{56}Fe, ^{19}F, and ^{11}B. These reactions are due to the presence of the corresponding elements either in the backing material (Na, F, B) or in mechanical parts of the entire setup (Al, Fe).

In Fig. 2, one observes additional γ peaks. These arise from proton-induced reactions on oxygen isotopes contained in the ^{116}Sn O$_2$ target material. Furthermore, peaks labeled with "X" in both figures are background γ rays observed in almost all (p,γ) reactions we have investigated previously, while some weak γ lines marked with a question mark (?) have an unknown origin.

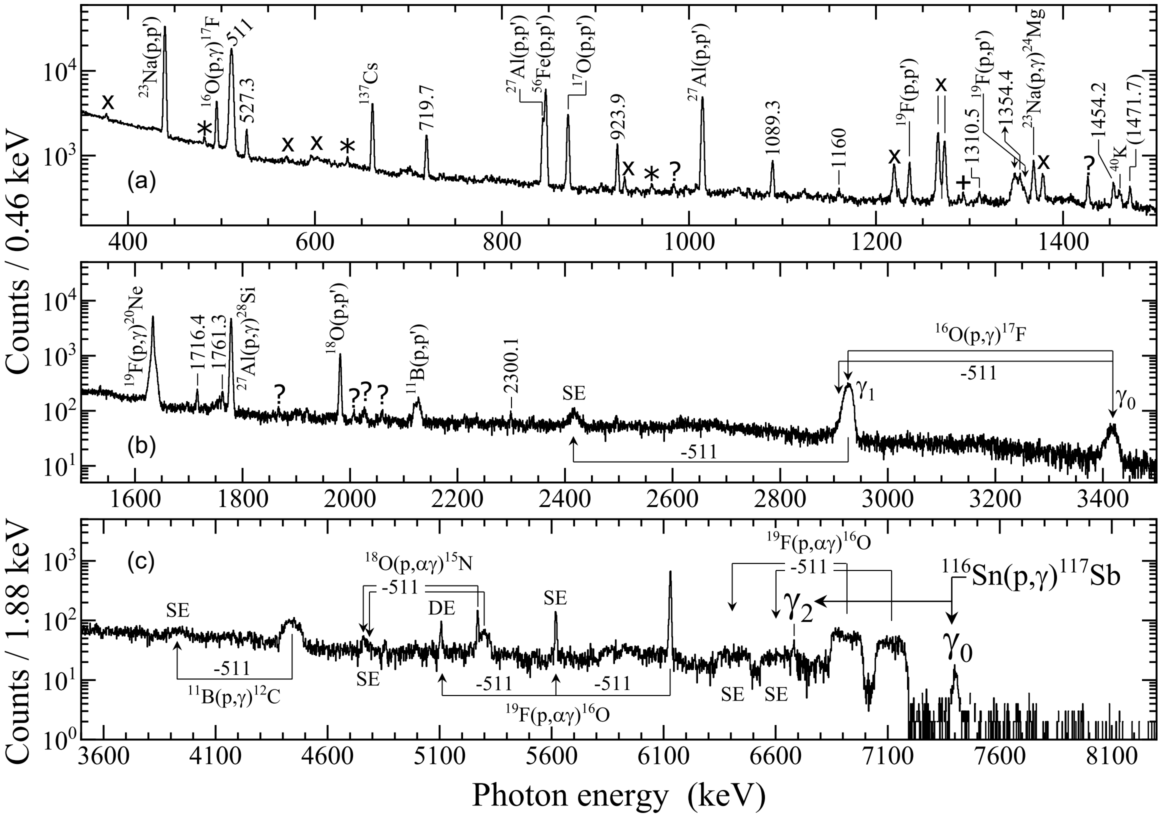

FIG. 2. Typical γ-singles spectrum measured at $E_p = 3$ MeV for the $^{116}\mathrm{Sn}(p,\gamma)\,^{117}\mathrm{Sb}$ reaction with the Ge detector placed at 90° with respect to the beam axis. The accumulated beam charge Q was 50 mC. Single- or double-escape peaks are marked with SE and DE, respectively. The γ transitions contained in the spectrum are explained in the text.

B. Measurements with the 4π γ-summing method

In addition to the γ-angular distributions, angle-integrated γ-singles spectra were also measured in this work using the 4π γ-summing technique [2,14]. Similar to our previous measurements, we utilized the same 12 in. × 12 in. cylindrical NaI(Tl) detector with a borehole of 35 mm diameter along its axis. The solid angle covered by the detector is ≈98% of 4π for photons emitted at its center, where the target is placed.

The main advantages of the 4π γ-summing technique are that (a) at each energy, one only needs to measure one spectrum instead of at least five, which are usually required to obtain a γ-angular distribution using HPGe detectors, and (b) from the γ transitions contained in this spectrum, only one peak, known as the sum peak, needs to be analyzed. This peak results from the summation of all the γ cascades leading to the ground state. Therefore, there is no need to analyze the numerous γ transitions contained in every spectrum obtained from γ-angular distribution measurements. Additional details about the 4π γ-summing technique and the experimental setup with the detector used in the present measurements can be found in Refs. [2,14].

Figures 4 and 5 depict typical angle-integrated γ-singles spectra measured with the 4π γ-summing technique for the $^{116}\mathrm{Sn}(p,\gamma)\,^{117}\mathrm{Sb}$ and $^{118}\mathrm{Sn}(p,\gamma)\,^{119}\mathrm{Sb}$ reactions, respectively. In Fig. 4, the peak at 8373 keV, marked with "Σ_0", is the sum peak of interest. The spectrum also includes the well-known room background γ transitions at 1461 and 2614 keV and a strong γ line at ≈2.23 MeV resulting from the $\mathrm{H}(n,\gamma)\mathrm{D}$ reaction (where D denotes ^{2}H), i.e., from the capture of (thermalized) neutrons by hydrogen present in the surrounding materials, while the neutrons are produced at different locations by the 4-MeV incoming proton beam.

The spectrum shown in Fig. 4 also comprises peaks from proton-induced reactions on oxygen isotopes and ^{19}F, which are present in the target and backing material, respectively. The associated single-escape peaks are marked with "SE". The peak Σ_0 at ≈4.36 MeV is the sum peak of the $^{16}\mathrm{O}(p,\gamma)\,^{17}\mathrm{F}$ reaction, i.e., it is the peak resulting from the summing of all the γ transitions depopulating the entry state of the produced ^{17}F and feeding its ground state through γ cascades. The peak at ≈3.1 MeV (labeled $\mathrm{I}\Sigma_2$) also arises from the $^{16}\mathrm{O}(p,\gamma)\,^{17}\mathrm{F}$ reaction; however, it is the result of incomplete summing of the γ-cascade formed by the successive γ transitions with energies 2609 and 495 keV, depopulating the first two excited states of ^{17}F. A similar case of incomplete summation was reported in [17].

C. Activation measurements

For the $^{116}\mathrm{Sn}(p,\gamma)\,^{117}\mathrm{Sb}$ reaction we also conducted cross-section measurements using the activation technique at three bombarding energies, as listed in Table I. A typical γ activity

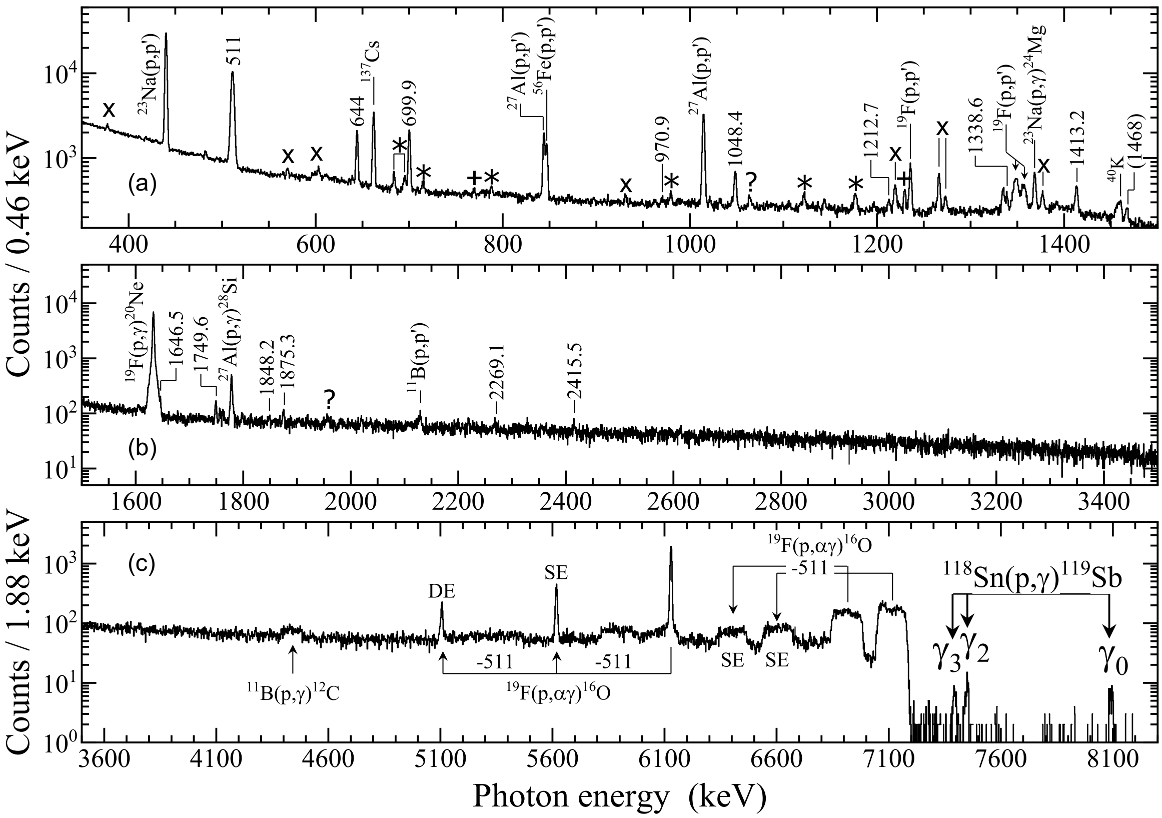

FIG. 3. Same as in Fig. 2 but for the ^{118}Sn(p, γ)^{119}Sb measured at $E_p = 3$ MeV with $Q = 42$ mC.

spectrum is shown in Fig. 6. This spectrum was accumulated for ≈ 50 min following a 6.1-hour-irradiation of the ^{116}Sn O$_2$ target with 3.5-MeV protons. In addition to the 511-keV γ peak and its Compton-induced background, Fig. 6 also contains the strong 158.6-keV γ transition emitted by the first excited state ($J^\pi = 3/2^+$) of the ^{117}Sn isotope, which is populated through the decay of its parent nucleus ^{117}Sb. The x rays appearing in the spectrum originate from the lead bricks used to shield the HPGe detector.

The chamber employed for the necessary irradiations is described in detail in Refs. [2,19]. For the counting of the γ activities after irradiation, an HPGe detector with a relative

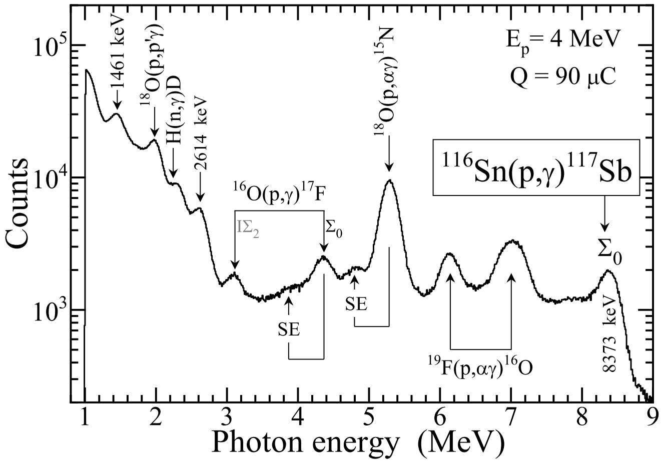

FIG. 4. Angle-integrated γ spectrum measured at a proton beam energy $E_p = 4$ MeV for the ^{116}Sn(p, γ)^{117}Sb reaction by accumulating a beam charge Q = 90 μC. The sum peak of interest is located at 8.373 MeV. The γ transitions contained in the spectrum are explained in the text.

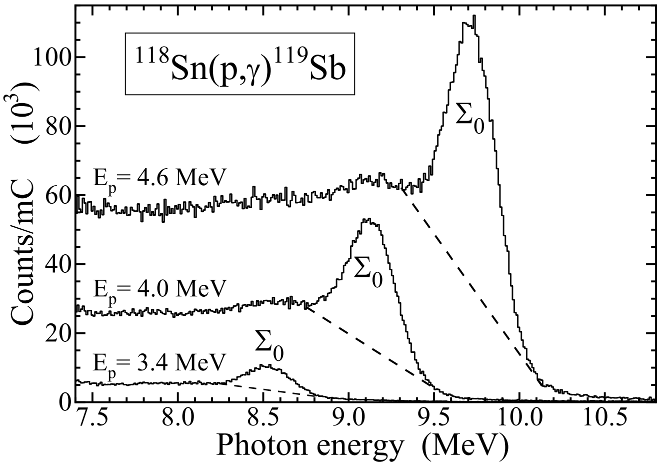

FIG. 5. High-energy part of angle-integrated γ spectra measured at proton beam energies 4.9, 4, and 3.4 MeV for the ^{118}Sn(p, γ)^{119}Sb reaction. The corresponding sum peaks are marked as Σ_0. The dashed lines indicate typical linear fits of the background subtracted from the corresponding sum peak.

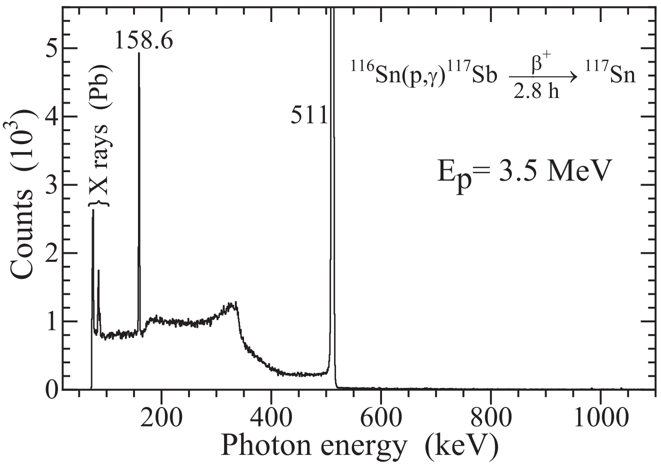

FIG. 6. γ-activity spectrum measured after a 6.1-hours-long irradiation of a 95.74%-enriched ^{116}Sn target with a proton beam of 3.5 MeV and a beam current of ≈1 μA (see also text).

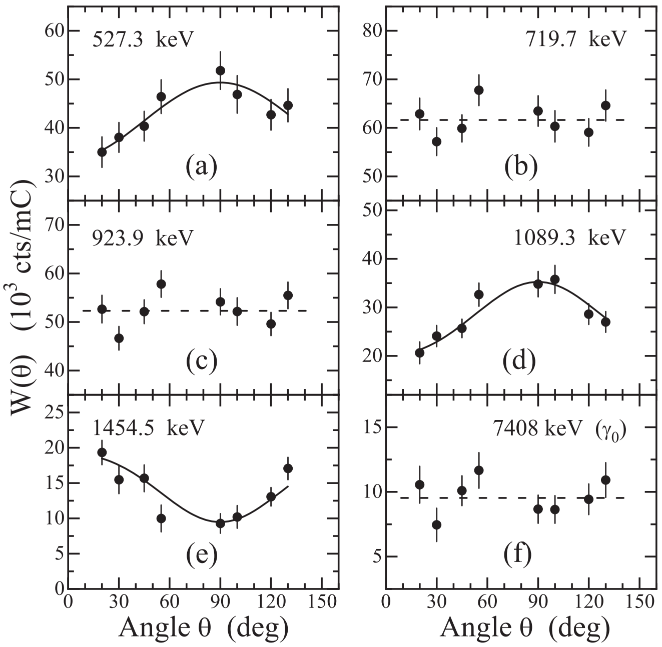

FIG. 7. Typical angular distributions of γ transitions of ^{117}Sb measured at $E_p = 3$ MeV (see text for details).

efficiency of 55% was used. It was shielded with 5-cm-thick lead bricks and positioned at ≈15 cm from the irradiated targets. Its absolute efficiency was determined using a calibrated ^{152}Eu radioactive source placed at the same sample position to ensure the same geometry conditions as in the activity measurements. For the 158.6-keV γ transition that was used to determine the cross section, we obtained an absolute efficiency $\varepsilon_{\text{abs}} = 0.0144 \pm 0.00175$.

Water cooling was applied during all irradiations to prevent material loss of the targets. To monitor the thickness and stability of the targets, RBS spectra were measured at frequent intervals using a 300-μm-thick Si surface-barrier detector placed inside the chamber at a distance of ≈30 cm from the target and at an angle $\theta = 170^\circ$ with respect to the beam direction. By comparing the different RBS spectra, it was found that target deterioration effects were kept below 5%.

The irradiation times at the measured proton energies $E_p =$ 2.3, 2.45, and 3.5 MeV, were 8.5, 6.3, and 6.1 hours, respectively. The corresponding total accumulated charges, Q, were 29.6, 16.8, and 14.3 mC. Q was measured with a current integrator (CI) and was subsequently digitized and recorded in multichannel scaling mode (MCS) within short time intervals Δt, using a "multiscaler" electronic unit connected directly after the CI. This setup allowed us to monitor the beam stability and correct for fluctuations in the beam flux during subsequent data analysis. The uncertainty of the CI reading was ≈3%. To ensure reliable current integration, a suppression voltage of −300 V was applied to suppress electrons emitted by the target and the beam collimator located at the entrance of the chamber.

III. DATA ANALYSIS AND RESULTS

As described in [2], the total reaction cross section σ_{T} is derived from the total reaction yield Y_{T} using

$$\sigma_{\text{T}} = \frac{A}{N_A}\frac{Y_{\text{T}}}{\xi}, \tag{1}$$

where A is the atomic weight in amu of the target used, N_A is the Avogadro number, and ξ is the target "thickness" (radial density). In a (p,γ) reaction, the total reaction yield Y_{T} is the absolute number of photons emitted by the reaction per impinging proton.

A. γ-angular distribution measurements

In the case of γ-angular distribution measurements, the total yield Y_{T} was determined at each beam energy by summing the yields Y of all N γ transitions that feed into the ground state of the produced compound nucleus. This sum is obtained by adding the absolute intensities A_0 of the corresponding angular distributions, using

$$Y_{\text{T}} = \sum_i^N Y_i = \sum_i^N A_{0,i} \tag{2}$$

When considering a single γ transition, i.e., when i=1 in Eq. (2), then Eq. (1) yields the corresponding *partial* cross section.

The γ-angular distributions measured in the present work were acquired by recording γ-singles spectra at eight different angles θ with respect to the beam direction. These spectra were subsequently analyzed by following the procedures described in detail in [2,19,22]. Typical angular distributions of γ transitions depopulating excited levels in ^{117}Sb and ^{119}Sb are plotted in Figs. 7 and 8, respectively. All these γ-angular distributions were measured at a proton-beam energy $E_p = 3$ MeV.

As shown in these figures, the angular distribution effects for some γ-transitions were not significant. In such cases, the necessary A_0 coefficients were derived, as detailed in [19], by calculating the weighted mean of the data points from

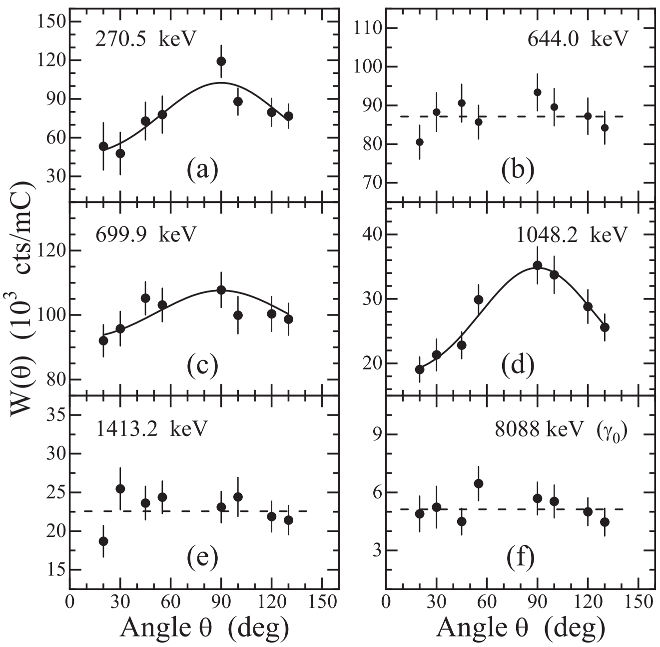

FIG. 8. Same as in Fig. 7 but for ^{119}Sb.

the corresponding γ-angular distribution. Consequently, the dashed horizontal lines displayed in Figs. 7 and 8 indicate the value for the respective $A_{0,i}$ coefficient used in Eq. (2).

Equation (2) can be applied using the primary γ transitions that deexcite the entry state of the produced compound nucleus. However, to prevent systematic errors arising from weak, and therefore undetectable, primary γ lines that may populate high-lying discrete levels and to address uncertainties in the level schemes, especially when dealing with high excitation energies, our data analysis of the γ-angular distribution measurements was based on the absolute intensities of the γ transitions feeding the ground state. This includes the primary γ_0 transition and all secondary γ rays feeding the ground state directly. As a result, the γ transitions considered in obtaining the total cross section of the $^{116}\mathrm{Sn}(p,\gamma)^{117}\mathrm{Sb}$ and $^{118}\mathrm{Sn}(p,\gamma)^{119}\mathrm{Sb}$ reactions using Eqs. (2) and (1), are depicted in Figs. 9 and 10, respectively.

The experimental *total* cross sections σ_T and the corresponding *partial* cross sections, determined in the present work from γ-angular distributions for the $^{116}\mathrm{Sn}(p,\gamma)^{117}\mathrm{Sb}$ and $^{118}\mathrm{Sn}(p,\gamma)^{119}\mathrm{Sb}$ reactions are plotted in Figs. 11 and 12, respectively.

The values of these cross sections are summarized in Tables II and III. All cross sections along with the corresponding *total* astrophysical S factors given in these tables have been corrected for laboratory screening effects, using an electron screening potential $U_e \approx 300$ eV, which is the weighted mean of the experimentally determined laboratory screening potentials reported in [27–31] for the $d + d$ fusion reaction in metals. For this correction, the measured cross sections were divided by a screening correction factor f_s calculated as described in [15,17].

Since different screening prescriptions have been suggested in the literature, and, furthermore, the value of U_e cannot be estimated accurately at present, we explicitly provide our adopted screening correction factor values in the third column of of Tables II and III. The *total* astrophysical S factors, S_T, given in these tables were determined from the electron-screening-corrected *total* cross sections σ_T using

$$S(E) = \sigma(E)\, E\, e^{2\pi\eta(E)}, \tag{3}$$

where $\eta(E)$ is the Sommerfeld parameter [32].

The $E_\mathrm{c.m.}$ values given in Tables II and III are the corresponding effective beam energies E_eff in the center-of-mass system deduced from

$$E_\mathrm{eff} = E_p - \frac{\Delta E}{2}, \tag{4}$$

where E_p is the incident proton beam energy and $\Delta E/2$ is its energy loss at the center of the target (see Table I).

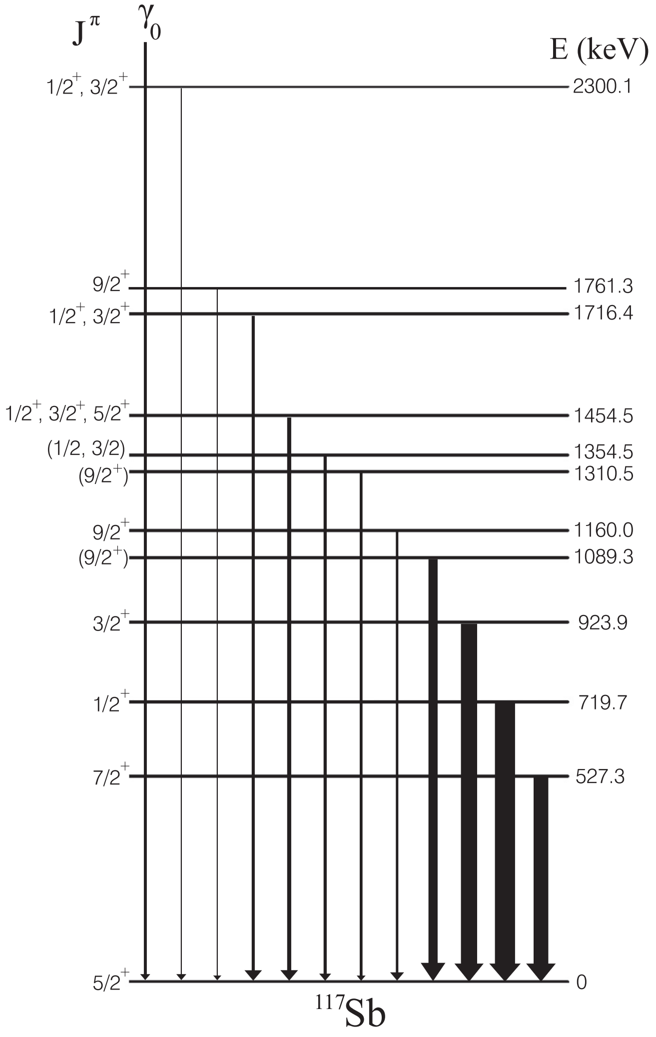

FIG. 9. Level scheme of the ^{117}Sb nucleus containing all the γ transitions (vertical arrows) used to determine the total cross section σ_T of the $^{116}\mathrm{Sn}(p,\gamma)^{117}\mathrm{Sb}$ reaction. The excitation energies in keV, indicated at the right of the levels as well as the spins and parities shown on their left, were taken from [26]. The thickness of the arrows correspond to the absolute intensities of the γ transitions, measured at $E_p = 3$ MeV.

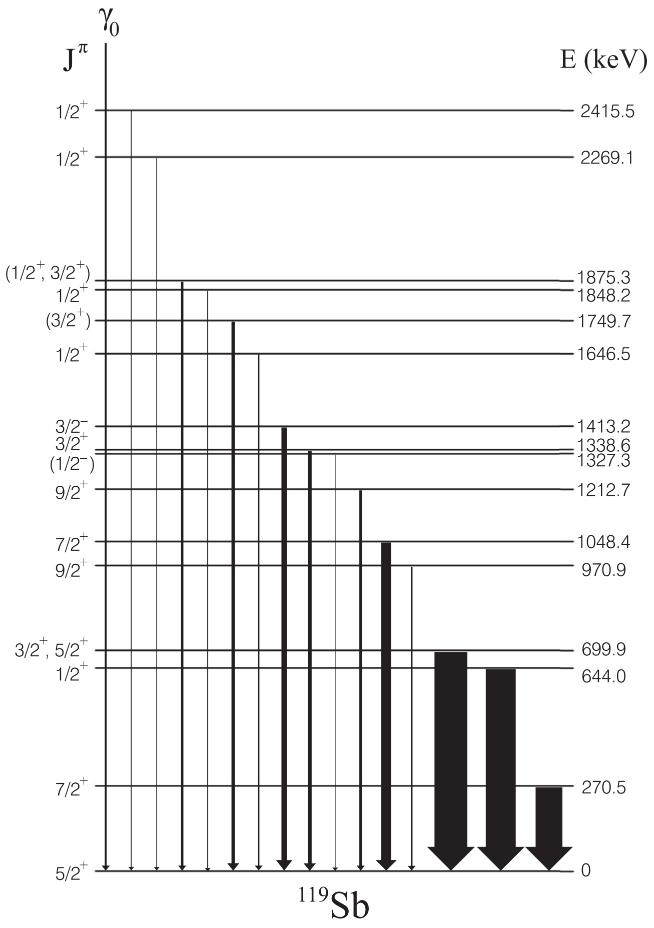

FIG. 10. Same as in Fig. 9 but for ^{119}Sb.

The errors given in Tables II and III for the screening-corrected total cross sections σ_T and the corresponding S factors, S_T, range between 7.3% and 20%. These errors result from the propagation of uncertainties in the *partial* cross sections, which were summed to yield the total values. These uncertainties result from errors in the (a) charge Q accumulated at the relevant beam energies ($\approx$3%), (b) detector efficiency ϵ_γ ($\approx$5%), (c) target thickness ($\approx$7% or 12%, depending on the target used), and (d) statistics. In the case of the $^{116}\mathrm{Sn}(p,\gamma)^{117}\mathrm{Sb}$ reaction the statistical errors in the *partial* cross sections range from $\approx$16% to $\approx$48% for the very weak γ transitions. In the case of the $^{118}\mathrm{Sn}(p,\gamma)^{119}\mathrm{Sb}$ reaction, the corresponding errors range from $\approx$9% to $\approx$48%.

B. Measurements with the 4π γ-summing method

In the case of the 4π γ-summing method, Eq. (2) is modified as

$$Y_\mathrm{T} = \frac{I_\Sigma}{N_b \varepsilon_{_\Sigma}}, \tag{5}$$

where I_Σ is the net area under the sum peak, N_b is the number of the beam particles, and $\varepsilon_{_\Sigma}$ is the absolute efficiency of the sum peak.

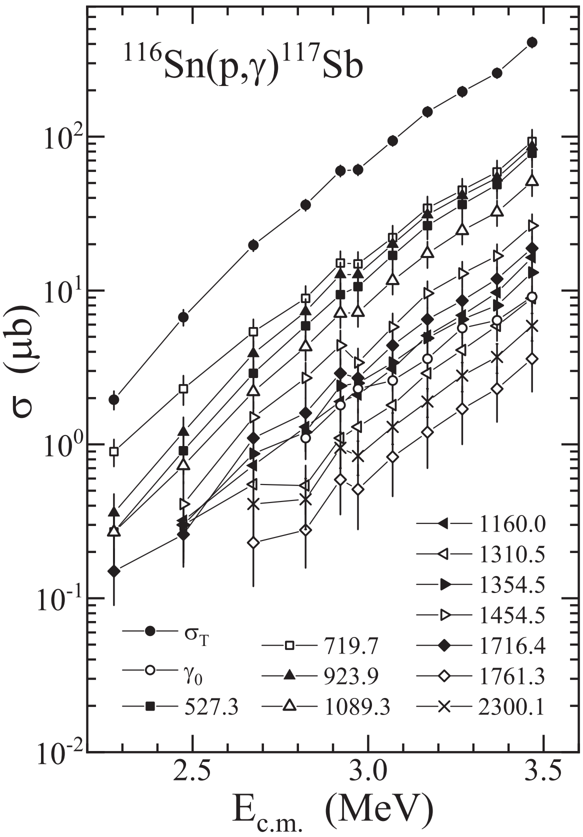

FIG. 11. Partial cross sections measured for all the γ transitions populating the ground state of ^{117}Sb. Their energies in keV and the corresponding symbols in the plot are given in the legend. The spins and parities of the levels depopulated by these transitions are given in Fig. 9. The partial cross section γ_0 refers to the primary γ transition from the entry to the ground state and σ_T is the total cross section. The data are corrected for electron screening (see also text).

Applying Eq. (5) requires accurate knowledge of $\varepsilon_{_\Sigma}$ which is not only energy- but also γ-multiplicity dependent. To address this, we developed a specialized procedure known as "in-out" technique to obtain the "average" multiplicity $\langle M \rangle$ of the γ cascades detected and summed by the specific NaI(Tl) detector. With this information, we can then derive $\varepsilon_{_\Sigma}$ with Monte Carlo simulations.

This procedure has been utilized in numerous experiments, allowing us to conclude that the sum-peak efficiency $\varepsilon_{_\Sigma}$ decreases exponentially with increasing sum-peak energy E_Σ. This decrease can be described by

$$\varepsilon_{_\Sigma} = \varepsilon_0 + \alpha \exp(-E_\Sigma/\beta), \tag{6}$$

where the values of the coefficients ε_0, α and β are specific to the detector and depend on whether the compound nucleus produced by the capture reaction is even-even, even-odd or odd-odd. The steps for the data analysis of an experiment conducted using the 4π γ-summing method, which were also applied in the present work, are described in detail in Refs. [2,14,20].

The experimental *total* cross sections σ_T and the *total* astrophysical S factors, S_T, determined in the present work

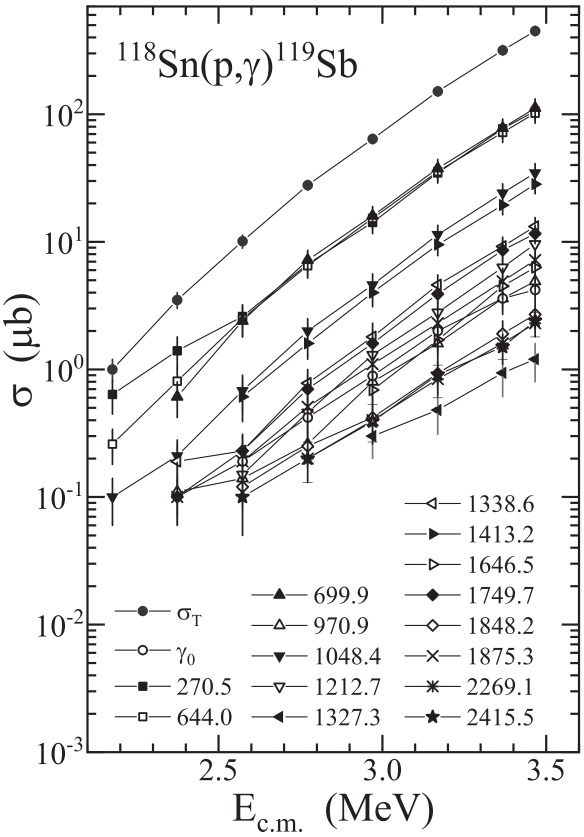

FIG. 12. Same as in Fig. 11 but for the ^{118}Sn(p, γ)^{119}Sb reaction. The spins and parities of the levels depopulated by the displayed γ transitions are given in Fig. 10.

using the 4π γ-summing technique for the ^{116}Sn(p, γ)^{117}Sb and ^{118}Sn(p, γ)^{119}Sb reactions are summarized in Tables IV and V, respectively. The center-of-mass energies given in these tables were also calculated with Eq. (4). All cross sections and astrophysical S factors given in these tables, have also been corrected for screening effects, as described in Sec. III A.

The errors presented in Tables IV and V for the screening-corrected total cross sections σ_T and their corresponding S factors, S_T, range between 13.9% and 20.3%. These errors result from the propagation of uncertainties in the (a) charge Q ($\approx$3%), accumulated at the relevant beam energies measured, (b) absolute sum-peak efficiency ε_Σ ($\approx$ 9% to 16%), (c) target thickness ($\approx$10% or 12%, depending on target used), and (d) statistics ($\leqslant$ 2%).

C. Activation measurements

In activation measurements, the cross section of the reaction in consideration is derived from

$$\sigma = \frac{\lambda N_\mathrm{D}^0}{N_i^0(1 - e^{-\lambda \Delta t})\left[\sum_{j=1}^{n} \Phi_j e^{-(n-j)\lambda \Delta t}\right]}, \qquad (7)$$

where λ is the decay constant of the produced unstable "mother" nuclei, N_D^0 the number of the "daughter" nuclei produced during irradiation within a certain irradiation time, N_i^0 the number of the target nuclei of the isotope under investigation in at/cm^2, Φ_j the flux of the proton beam during the jth irradiation time interval Δt, and n the total number of the irradiation time intervals (bins).

N_D^0 can be derived from the absolute yield, which is calculated using the net counts under the peak of at least one of the γ transitions that depopulate an excited state of the daughter nucleus. In this calculation we took into account corrections for dead time, absolute efficiency, cascade summing, and possible pile-up effects.

Self-absorption corrections were not required in our case as the Sn targets were sufficiently thin. Additionally, the HPGe detector was positioned 15 cm away from the target surface during off-beam activity measurements. Consequently, cascade summing and pile-up effects were deemed negligible.

To determine the cross section of the ^{116}Sn(p, γ)^{117}Sb reaction, we used the absolute intensity of the 158.56-keV γ transition, which depopulates the $3/2^+$ excited level of the daughter nucleus ^{117}Sn, populated through the β^+ decay of the mother nucleus ^{117}Sb. In our analysis, we adopted the relative intensity per decay of 86.4% that is provided in [26] for the 158.56-keV γ transition.

The screening-corrected total cross sections σ_T and the corresponding screening-corrected total astrophysical S factors determined in the present work with the activation technique for the ^{116}Sn(p, γ)^{117}Sb reaction are given in Table IV. The corresponding relative errors range between 15% and 17%. They are the result of uncertainties in statistics (5–8%), target thickness (6% and 10% for the thinner one), current integration (3%) and absolute efficiency (12%) of the HPGe detector for the 158.6-keV γ transition.

IV. DISCUSSION

As mentioned in Sec. I, optical model potentials (OMPs), nuclear level densities (NLDs) and γ-ray strength functions (γSFs) are key input parameters in statistical model (HF) calculations. These nuclear properties can be described using either phenomenological or (semi)microscopic models.

HF calculations can be carried out using well-established nuclear reaction codes, such as TALYS [33,34], EMPIRE [35], NON-SMOKER$^{\mathrm{WEB}}$ [36], and its updated version, SMARAGD [37]. All of these codes incorporate different OMP, NLD, and γSF models, including both (semi)microscopic or phenomenological ones. Calculations using the latter models often demonstrate very good agreement with experimental data, making them suitable for HF calculations in various mass regions, particularly those within or near the valley of stability.

On the other hand, microscopic or semimicroscopic models hold particular significance in statistical model calculations. This is because they properly take into account fundamental nuclear structure phenomena such as the spin-orbit interaction, pairing, and nuclear deformation. These models are based on the principles of quantum mechanics and the strong nuclear force, which govern the interactions between nucleons within the nucleus. In contrast, phenomenological models rely on analytical formulas, often involving various and, at times, drastic approximations.

TABLE II. Screening-corrected cross sections determined in the present work from γ-angular distribution measurements of the $^{116}\mathrm{Sn}(p,\gamma)^{117}\mathrm{Sb}$ reaction. E_p, the proton beam energy in the laboratory system, and $E_{\mathrm{c.m.}}$, in the center-of-mass system, are given in the first and second columns, respectively. The screening correction factors f_s are given in the third column. For the *partial* cross sections the symbol $\sigma(i)$ is used, with i referring to the energy in keV of the relevant γ transition. The screening-corrected *total* cross section and the *total* S factor are indicated with σ_{T} and S_{T}, respectively. The uncertainty in E_p is $\leqslant$5 keV.

E_p (MeV)	$E_{\mathrm{c.m.}}$ (MeV)	f_s	$\sigma(527.3)$ (μb)	$\sigma(719.7)$ (μb)	$\sigma(923.9)$ (μb)	$\sigma(1089.3)$ (μb)	$\sigma(1160.0)$ (μb)	$\sigma(1310.5)$ (μb)	$\sigma(1354.5)$ (μb)
2.30	2.276	1.114	0.27 ± 0.12	0.90 ± 0.18	0.36 ± 0.12	0.27 ± 0.10			
2.50	2.474	1.100	0.91 ± 0.27	2.3 ± 0.5	1.2 ± 0.3	0.73 ± 0.17	0.32 ± 0.12	0.30 ± 0.13	0.30 ± 0.14
2.70	2.673	1.089	2.9 ± 0.6	5.4 ± 1.1	3.9 ± 0.8	2.2 ± 0.5	0.73 ± 0.23	0.55 ± 0.21	0.87 ± 0.32
2.85	2.822	1.081	5.9 ± 1.2	8.9 ± 1.8	7.3 ± 1.5	4.3 ± 0.8	1.3 ± 0.4	0.54 ± 0.19	1.2 ± 0.4
2.95	2.921	1.077	9.4 ± 1.8	15.1 ± 2.9	12.7 ± 2.5	7.1 ± 1.4	1.9 ± 0.5	1.1 ± 0.4	2.4 ± 0.7
3.00	2.971	1.075	10.6 ± 2.1	14.9 ± 2.9	12.7 ± 2.4	7.2 ± 1.4	2.1 ± 0.5	1.3 ± 0.4	2.5 ± 0.6
3.10	3.070	1.071	16.9 ± 3.3	22.1 ± 4.3	20.0 ± 3.8	11.6 ± 2.2	3.1 ± 0.8	1.8 ± 0.5	3.4 ± 0.8
3.20	3.169	1.068	26.4 ± 4.9	34.3 ± 6.5	31.1 ± 5.8	17.4 ± 3.4	5.1 ± 0.9	2.9 ± 0.7	4.9 ± 1.1
3.30	3.268	1.065	36.2 ± 6.9	44.9 ± 8.4	41.4 ± 7.8	24.5 ± 4.6	6.9 ± 1.3	4.1 ± 0.9	6.5 ± 1.4
3.40	3.367	1.062	48.8 ± 9.3	59 ± 11	54 ± 10	32.3 ± 6.1	9.7 ± 1.9	5.9 ± 1.2	8.0 ± 1.6
3.50	3.467	1.059	78 ± 15	93 ± 18	86 ± 16	51 ± 10	16.4 ± 3.2	8.9 ± 1.8	13.1 ± 2.6

E_p (MeV)	$E_{\mathrm{c.m.}}$ (MeV)	f_s	$\sigma(1454.5)$ (μb)	$\sigma(1716.4)$ (μb)	$\sigma(1761.3)$ (μb)	$\sigma(2300.1)$ (μb)	$\sigma(\gamma_0)$ (μb)	σ_{T} (μb)	S_{T} (10^3 MeV b)
2.30	2.276	1.114		0.15 ± 0.06				1.95 ± 0.27	764692 ± 105880
2.50	2.474	1.100	0.41 ± 0.16	0.26 ± 0.08				6.7 ± 0.8	748504 ± 89374
2.70	2.673	1.089	1.5 ± 0.4	1.1 ± 0.3	0.23 ± 0.11	0.41 ± 0.16		19.7 ± 1.7	721225 ± 62238
2.85	2.822	1.081	2.7 ± 0.7	1.6 ± 0.4	0.28 ± 0.12	0.44 ± 0.16	1.1 ± 0.2	36 ± 3	619383 ± 51615
2.95	2.921	1.077	4.4 ± 1.1	2.9 ± 0.7	0.59 ± 0.24	0.95 ± 0.25	1.8 ± 0.3	60 ± 5	646034 ± 53836
3.00	2.971	1.075	3.4 ± 0.8	2.7 ± 0.6	0.51 ± 0.23	0.84 ± 0.21	2.3 ± 0.4	61 ± 5	523134 ± 42880
3.10	3.070	1.071	5.8 ± 1.3	4.4 ± 0.9	0.83 ± 0.37	1.3 ± 0.3	2.6 ± 0.4	94 ± 7	522507 ± 38910
3.20	3.169	1.068	9.6 ± 1.9	6.5 ± 1.2	1.2 ± 0.5	1.9 ± 0.4	3.6 ± 0.5	145 ± 11	533493 ± 40472
3.30	3.268	1.065	12.9 ± 2.5	8.6 ± 1.7	1.7 ± 0.7	2.8 ± 0.6	5.7 ± 0.8	196 ± 15	486661 ± 37244
3.40	3.367	1.062	16.8 ± 3.2	11.9 ± 2.3	2.3 ± 0.9	3.7 ± 0.8	6.4 ± 0.9	259 ± 19	441839 ± 32413
3.50	3.467	1.059	26.4 ± 4.9	18.8 ± 3.7	3.6 ± 1.4	5.9 ± 1.2	9.1 ± 1.3	410 ± 31	486880 ± 36813

For these reasons, (semi)microscopic models are expected to be "globally" applicable, meaning they can provide reliable results for nuclear reactions occurring across various mass regions of the chart of isotopes without requiring "local" adjustments. Due to this "global" character, (semi)microscopic models hold special significance for p-process abundance calculations. This is because p process involves nearly 2000 isotopes spanning a broad mass range, from Ge to Bi, and numerous nuclear reactions occurring far from the valley of stability.

Considering these factors, the data measured in the present work were used not only for comparison with standard statistical model calculations but also to investigate the "global" applicability of the semimicroscopic OMP, NLD, and γSF models, with particular emphasis on the Lane-consistent semimicroscopic OMP developed by Bauge *et al.* [38,39], hereafter abbreviated as "JLM/B."

A. Comparison of experimental results with standard TALYS calculations

In our last (p,γ) cross-sections paper on Sr isotopes [22], we used the version 1.95 of the statistical model code TALYS [33,34]. In the present work we have employed version 1.96 of TALYS. In addition to the two nucleon-nucleus OMPs, i.e., the phenomenological model of Koning and Delaroche [40], hereafter abbreviated as "KD," and the JLM/B of Bauge, Delaroche, and Girod [38,39], TALYS 1.96 offers a comprehensive portfolio of models. This includes eight models for the α-particle–nucleus OMP (α-OMP), six different NLD, and 12 γSF models (nine for $E1$ and three for $M1$ γ transitions). All 28 models are listed in Table VI, resulting in a total of 1152 model combinations available for HF calculations.

TALYS 1.96 incorporates recent improvements in γSF models, particularly the new phenomenological simplified modified Lorentzian (SMLO) model proposed by Goriely *et al.* [62,63] for $E1$ and $M1$ γ-ray transitions, as well as updated tables for $E1$ and $M1$ γSFs from temperature-dependent HFB plus QRPA calculations using the D1M Gogny force [33,68,69] (model abbreviated as "HFB/T/QRPA/G" in Table VI).

It is worth noting that, in their recent TALYS paper [33], Koning *et al.* "specifically recommend" two γSF models, namely SMLO and HFB/T/QRPA/G, as they are consistent from the physics perspective and can be considered "the two best options" for TALYS calculations. They also regard the Skyrme-HFB NLD model [54,55], abbreviated as HFB/Sk in Table VI, as the "most robust" one for similar reasons.

In our TALYS 1.96 calculations, we employed various combinations of purely phenomenological and semi-microscopic

TABLE III. Same as in Table II but for the ^{118}Sn$(p,\gamma)^{119}$Sb reaction.

E_p (MeV)	$E_{\mathrm{c.m.}}$ (MeV)	f_s	$\sigma(270.5)$ (μb)	$\sigma(644.0)$ (μb)	$\sigma(699.9)$ (μb)	$\sigma(970.9)$ (μb)	$\sigma(1048.4)$ (μb)	$\sigma(1212.7)$ (μb)
2.2	2.176	1.123	0.64 ± 0.19	0.26 ± 0.08			0.10 ± 0.04	
2.4	2.374	1.107	1.4 ± 0.4	0.81 ± 0.23	0.61 ± 0.19	0.11 ± 0.04	0.21 ± 0.07	
2.6	2.573	1.094	2.6 ± 0.6	2.5 ± 0.7	2.4 ± 0.6	0.14 ± 0.05	0.68 ± 0.22	0.15 ± 0.06
2.8	2.772	1.084	6.7 ± 1.5	6.5 ± 1.2	7.2 ± 1.4	0.26 ± 0.08	2.0 ± 0.5	0.46 ± 0.15
3.0	2.970	1.075	14.2 ± 2.6	15.3 ± 2.7	16.0 ± 2.9	0.80 ± 0.26	4.6 ± 0.9	1.3 ± 0.4
3.2	3.169	1.068	34.7 ± 5.8	35.6 ± 5.9	37.6 ± 6.7	1.6 ± 0.4	11.4 ± 2.1	2.8 ± 0.7
3.4	3.367	1.062	77 ± 13	72 ± 12	78 ± 14	3.6 ± 0.7	24.1 ± 4.4	6.3 ± 1.3
3.5	3.466	1.059	106 ± 17	102 ± 17	112 ± 20	4.9 ± 0.9	34.7 ± 6.4	9.6 ± 1.7

E_p (MeV)	$E_{\mathrm{c.m.}}$ (MeV)	f_s	$\sigma(1327.3)$ (μb)	$\sigma(1338.6)$ (μb)	$\sigma(1413.2)$ (μb)	$\sigma(1646.5)$ (μb)	$\sigma(1749.7)$ (μb)	$\sigma(1848.2)$ (μb)
2.2	2.176	1.123						
2.4	2.374	1.107		0.19 ± 0.08			0.10 ± 0.04	
2.6	2.573	1.094		0.23 ± 0.07	0.61 ± 0.22		0.23 ± 0.08	0.12 ± 0.04
2.8	2.772	1.084		0.78 ± 0.22	1.6 ± 0.4		0.70 ± 0.22	0.25 ± 0.08
3.0	2.970	1.075	0.30 ± 0.10	1.8 ± 0.5	4.0 ± 0.9	0.69 ± 0.23	1.6 ± 0.4	0.42 ± 0.14
3.2	3.169	1.068	0.48 ± 0.17	4.6 ± 0.9	9.5 ± 1.7	1.7 ± 0.4	3.9 ± 0.9	0.93 ± 0.23
3.4	3.367	1.062	0.94 ± 0.33	9.2 ± 1.7	19.4 ± 3.1	4.5 ± 1.0	8.6 ± 1.7	1.9 ± 0.5
3.5	3.466	1.059	1.2 ± 0.4	13.2 ± 2.3	28.3 ± 4.5	6.3 ± 1.4	11.6 ± 1.9	2.7 ± 0.6

E_p (MeV)	$E_{\mathrm{c.m.}}$ (MeV)	f_s	$\sigma(1875.3)$ (μb)	$\sigma(2269.1)$ (μb)	$\sigma(2415.5)$ (μb)	$\sigma(\gamma_0)$ (μb)	σ_{T} (μb)	S_{T} (10^3 MeV b)
2.2	2.176	1.123					1.0 ± 0.2	791497 ± 158299
2.4	2.374	1.107	0.10 ± 0.04				3.5 ± 0.5	724286 ± 103469
2.6	2.573	1.094	0.19 ± 0.07		0.10 ± 0.05	0.19 ± 0.07	10.1 ± 1.2	638543 ± 75867
2.8	2.772	1.084	0.51 ± 0.17	0.20 ± 0.07	0.20 ± 0.07	0.42 ± 0.14	27.8 ± 2.5	613298 ± 55153
3.0	2.970	1.075	1.1 ± 0.3	0.40 ± 0.13	0.39 ± 0.13	0.89 ± 0.29	64 ± 5	552492 ± 43163
3.2	3.169	1.068	2.3 ± 0.6	0.84 ± 0.24	0.91 ± 0.28	2.0 ± 0.6	151 ± 11	556698 ± 40554
3.4	3.367	1.062	4.9 ± 1.3	1.6 ± 0.4	1.5 ± 0.4	3.6 ± 0.9	317 ± 24	541850 ± 41023
3.5	3.466	1.059	7.2 ± 1.2	2.3 ± 0.5	2.4 ± 0.6	4.2 ± 0.9	449 ± 33	536126 ± 39403

models, as listed in Table VII. The recommended γSF and NLD models by Koning *et al.* [33] were used in the combinations TALYS-default, TALYS-6, and TALYS-7.

As shown in Table VII, the combinations TALYS-default, TALYS-0.1, TALYS-0.2 and TALYS-0.3 consist of purely phenomenological models. All four combinations use the same p-OMP of Koning and Delaroche [40], the α-OMP of Avrigeanu *et al.* [44], and the TALYS specific constant temperature Fermi gas model for NLDs [33]. However, they differ in their choice of γSF models.

The TALYS-default combination employs the simplified modified Lorentzian (SMLO) γSF model [62,63] for describing both the $E1$ and $M1$ γ transitions. In contrast, TALYS-0.1, TALYS-0.2, and TALYS-0.3 all use the generalized Lorentzian γSF model by Kopecky and Uhl [59,60] for $M1$ γ-transitions but their choice of $E1$ γSF models varies, as indicated in Table VII.

TALYS-1 is a modification of TALYS-default, where the purely phenomenological KD OMP [40] is replaced by the semimicroscopic JLM/B OMP [38,39]. TALYS-1 was used in the present work for the specific purpose of assessing whether the predictive power of JLM/B is on par with the widely acclaimed, and almost routinely used, phenomenological KD p-OMP [40].

On the other hand, TALYS-2, TALYS-3, TALYS-4, and TALYS-5 utilize the phenomenological model of Kopecky and Uhl [59,60] for describing the γSF of $M1$ γ transitions. However, they can be considered self-consistent in terms of the microscopic models used to calculate the nuclear ground-state properties. Therefore, these combinations also are of particular interest for HF calculations.

It's noteworthy that both TALYS-2 and TALYS-3 have demonstrated very good agreement with our previously measured (p,γ) reaction cross sections on Sr [22] and Mo isotopes [20], respectively. As successful combinations, they could serve for comparison with the fully semimicroscopic TALYS-6 and TALYS-7, which, notably, are the only combinations that employ a consistent semimicroscopic description of the γSF of $M1$ γ transitions (see Table VII).

The screening-corrected S factors derived in the present work for the ^{116}Sn$(p,\gamma)^{117}$Sb reaction are compared in panels (a) and (b) of Fig. 13 with the corresponding TALYS 1.96 calculations. These calculations were carried out using the model combinations listed in Table VII, with the exception of TALYS-1.

S factors resulting from the measurements using the activation technique are indicated with black triangles, while

TABLE IV. Screening corrected total cross sections $\sigma_{\rm T}$ determined in the present work for the ^{116}Sn$(p,\gamma)^{117}$Sb reaction at various center-of-mass energies $E_{\rm c.m.}$ using the 4π γ-summing and the activation techniques. The corresponding screening correction factors f_s and the astrophysical S factors $S_{\rm T}$ are given in the third and fifth columns, respectively. The uncertainties in the incident proton beam energy E_p in the laboratory system are less than 5 keV.

E_p (MeV)	$E_{\rm c.m.}$ (MeV)	f_s	$\sigma_{\rm T}$ (μb)	$S_{\rm T}$ (10^3 MeV b)
Results obtained using the 4π γ-summing technique				
3.6	3.567	1.057	418 ± 65	350712 ± 54537
3.8	3.766	1.052	779 ± 120	342956 ± 52830
4.0	3.964	1.048	1172 ± 181	284809 ± 43985
4.2	4.162	1.045	1878 ± 290	263224 ± 40647
4.4	4.361	1.042	2890 ± 445	243004 ± 37418
4.6	4.559	1.039	4579 ± 706	239137 ± 36871
4.8	4.757	1.036	6701 ± 1033	224157 ± 34555
5.0	4.955	1.034	8741 ± 1349	192619 ± 29727
5.2	5.154	1.032	13473 ± 2252	200517 ± 33516
Results obtained from activation measurements				
2.3	2.272	1.114	1.8 ± 0.3	724266 ± 120711
2.45	2.422	1.103	4.6 ± 0.7	712124 ± 107431
3.5	3.469	1.059	305 ± 52	359962 ± 61293

those obtained with the 4π γ-summing method and from γ-angular distributions are depicted by black circles and black squares, respectively. The black curves plotted in panel (a) correspond to the S factors calculated using combinations of the purely phenomenological models given in Table VII.

TABLE V. Same as in Table IV but for the total cross section σ_T of the ^{118}Sn(p,γ) ^{119}Sb reaction determined using the 4π γ-summing technique.

E_p (MeV)	$E_{\rm c.m.}$ (MeV)	f_s	$\sigma_{\rm T}$ (μb)	$S_{\rm T}$ (10^3 MeV b)
2.6	2.574	1.094	10 ± 2	630052 ± 126010
2.8	2.772	1.084	27 ± 5	595304 ± 110242
3.0	2.971	1.075	63 ± 11	542453 ± 94714
3.2	3.169	1.068	131 ± 23	482883 ± 84781
3.4	3.367	1.062	278 ± 49	474373 ± 83612
3.6	3.566	1.057	557 ± 96	470346 ± 81065
3.8	3.764	1.052	957 ± 166	423795 ± 73511
4.0	3.963	1.048	1765 ± 305	431147 ± 74504
4.2	4.161	1.045	2559 ± 442	360391 ± 62248
4.3	4.260	1.043	3192 ± 551	346494 ± 59811
4.4	4.360	1.042	4066 ± 703	343345 ± 59363
4.5	4.459	1.040	4698 ± 812	311300 ± 53805
4.6	4.558	1.039	3887 ± 671	203770 ± 35176
4.7	4.657	1.038	3682 ± 635	153901 ± 26542
4.8	4.756	1.036	3226 ± 556	108303 ± 18666
4.9	4.856	1.035	3185 ± 550	86484 ± 14934
5.0	4.955	1.034	3091 ± 533	68335 ± 11783
5.1	5.054	1.033	3037 ± 523	55009 ± 9473
5.2	5.153	1.032	4447 ± 766	66388 ± 11435

In panel (b), the curves correspond to S factors obtained with the combinations of the semimicroscopic models of this table.

In both cases, the various TALYS calculations are depicted with different types of curves (solid, dashed, long-dashed, dotted, dashed-dotted, dashed-dotted-dotted) as indicated by the corresponding legends. The pairs of values given in parentheses in panels (b) and (d) indicate the values of the multiplicative factors f_V and f_W entering Eqs. (9) and (10), that are discussed below in Sec. IV B 1.

In panels (a) and (b) of Fig. 13, we also include the screening-corrected S factors obtained from the cross sections reported in [70,71], which are plotted as open rhombs and open triangles, respectively. These cross sections were measured using the activation technique, with an average relative error of ≈16%. While these S factors show reasonable agreement among themselves, they exhibit significant deviations from our results, including those obtained with the activation method (see Table I).

Overall, the S factors from Refs. [70,71] are consistently higher from our results by an overall factor of ≈1.45. Furthermore, they deviate notably, especially at energies below ≈ 3 MeV, from the corresponding values calculated with the TALYS 1.96 code, regardless of the model combinations used.

As depicted in panel (a) of Fig. 13, the TALYS calculations carried out with the phenomenological models specified in the legend notably deviate from our experimental data. It is worth noting that the TALYS-default and TALYS-0.3 combinations yield almost identical S factors within the energy range displayed in panel (a), differing by less than 4%. Additionally, TALYS-0.2 produces the highest S factors, a trend observed in many other (p,γ) reactions studied by our group. This can be considered a general observation when comparing HF calculations performed with phenomenological model combinations.

In panel (a) of Fig. 13, the TALYS-0.1 calculations tend to underestimate the experimental data. However, they appear to better capture the energy dependence of the data compared to other phenomenological combinations. In fact, an 18% increase in the TALYS-0.1 calculations, indicated by the long-dashed curve curve, leads to an excellent agreement with the data.

The different contributions of the three $E1$ γSF models of Kopecky and Uhl [59,60], Brink and Axel [57,58], and the hybrid model of Goriely [61] to the TALYS calculations become evident in panel (a) of Fig. 13 when comparing the curves representing the TALYS-0.1, TALYS-0.2, and TALYS-0.3 combinations, respectively. All three combinations employ the same OMPs, NLD, and $M1$ γSF (see Table VII).

In panel (b) of Fig. 13, the screening corrected S factors derived in the present work are compared with all the semimicroscopic combinations listed in Table VII. The numbers in parentheses following the notation of the different models in the legend indicate the default values of the TALYS built-in keywords “lvadjust” and “lwadjust.” These keywords are used to adjust the values of the isoscalar normalization factors λ_V and λ_W appearing in the general functional form of the JLM/B OMP, as detailed in Eq. (8) below.

In panel (b) of Fig. 13, all the “standard” semi-microscopic combinations, i.e., those with $(\lambda_V, \lambda_W) = (1, 1)$, fail to

TABLE VI. Nuclear input parameters (first column) and corresponding phenomenological or semimicroscopic models used in our TALYS 1.96 calculations. The proton–, neutron–, and alpha-particle–nucleus optical model potentials (OMPs) are indicated with p-OMP, n-OMP, and α-OMP, respectively. The model notation used for discussion in Sec. IV is given in parentheses. The listed models allow for calculating cross sections with 1152 model combinations. The shaded areas plotted in Fig. 14 have been obtained using all 576 possible model combinations of the phenomenological p/n-OMP of Koning and Delaroche [40].

Parameter	Phenomenological models	Semimicroscopic models
p/n-OMP	(1) (KD): Global model of Koning and Delaroche [40];	(2) (JLM/B): Spherical Lane consistent model of Bauge, Delaroche, and Girod [38,39];
α-OMP	(1) (WKD): TALYS-specific α-OMP; folding procedure of Watanabe and Madland [41,42] applied to KD OMP [40] (2) (McFS): α-OMP of McFadden and Satchler [43] (3) (Avr/I): α-OMP of Avrigeanu *et al.* [44] (4) (Nlt): α-OMP of Nolte *et al.* [45] (5) (Avr/II): α-OMP of V. Avrigeanu *et al.* [46]	(6) (αOMP/I): α-OMP of Demetriou *et al.* [47]; imaginary potential parameters as given in Table 1 of [47] (7) (αOMP/II): α-OMP of Demetriou *et al.* [47]; imaginary potential parameters as given in Table 2 of [47] (8) (αOMP/III): Dispersive α-OMP of Demetriou *et al.* [47]
NLD	(1) (CTFG): TALYS-specific version (see in [33]) of the constant temperature Fermi-gas model of Gilbert and Cameron [48] (2) (BSFG): Back-shifted Fermi-gas model [49,50] (3) (GSM): Generalized superfluid model of Ignatyuk *et al.* [51,52]	(4) (HFBCS): NLDs from a microscopic statistical model using the deformed Hartree-Fock Bardeen-Cooper-Schrieffer (HFBCS) predictions of the ground-state properties [53] (5) (HFB/Sk): NLDs from a combinatorial method using nuclear structure properties determined with the Hartree-Fock-Bogolyubov (HFB) model and the BSk14 Skyrme force [54,55] (6) (HFB/T/G): Temperature dependent NLDs from a combinatorial method using nuclear structure properties determined with a HFB model and the D1M Gogny force [56]
γSF	(1) (SLO): Brink-Axel standard Lorentzian [57,58]; for $E1$ transitions only (2) (GLO): Generalized Lorentzian of Kopecky and Uhl [59,60]; for $E1$ and $M1$ transitions (3) (HG): Hybrid model of Goriely [61]; for $E1$ transitions only (4) (SMLO): Simplified modified Lorentzian of Goriely *et al.* [62–64]; for $E1$ and $M1$ transitions	(5) (HFBCS/QRPA/Sk): γSFs from spherical HFBCS plus quasiparticle random phase approximation (QRPA) calculations based on the Skyrme SLy4 interaction [33,65]; for $E1$ transitions only (6) (HFB/QRPA/Sk): γSFs from spherical HFB plus QRPA model calculations based on the Skyrme BSk7 interaction; [33,66]; for $E1$ transitions only (7) (HFB/T/QRPA/Sk): γSFs from temperature dependent spherical HFB plus QRPA model calculations based on the Skyrme BSk7 interaction; [33,66]; for $E1$ transitions only (8) (RMF/T): γSFs from continuum random phase approximation (CRPA) temperature-dependent calculations based on a relativistic mean field (RMF) approach [33,67]; for $E1$ transitions only (9) (HFB/T/QRPA/G): γSFs from temperature-dependent HFB plus QRPA calculations using the D1M Gogny force [33,68,69]; for $E1$ and $M1$ transitions

TABLE VII. Model combinations of OMPs, NLDs, and γSFs used to calculate reaction cross sections using TALYS 1.96. In the first five combinations, the α-OMP of [44] was used. For the remaining six model combinations the αOMP/III [47] was adopted. The choice of the α-OMP is not expected to play a significant role at the energy region covered in the present (p, γ) measurements. The model abbreviations given in columns 2 to 5 are explained in Table VI.

Model combination abbreviation	p/n-OMP model	NLD model	$E1$ γSF model	$M1$ γSF model
TALYS-default	KD	CTFG	SMLO	SMLO
TALYS-0.1	KD	CTFG	KU	KU
TALYS-0.2	KD	CTFG	BA	KU
TALYS-0.3	KD	CTFG	HG	KU
TALYS-1	JLM/B	CTFG	SMLO	SMLO
TALYS-2	JLM/B	HFBCS	KU	KU
TALYS-3	JLM/B	HFB/Sk	KU	KU
TALYS-4	JLM/B	HFB/T/G	KU	KU
TALYS-5	JLM/B	HFB/T/G	RMF/T	KU
TALYS-6	JLM/B	HFB/Sk	HFB/T/QRPA/G	HFB/T/QRPA/G
TALYS-7	JLM/B	HFB/T/G	HFB/T/QRPA/G	HFB/T/QRPA/G

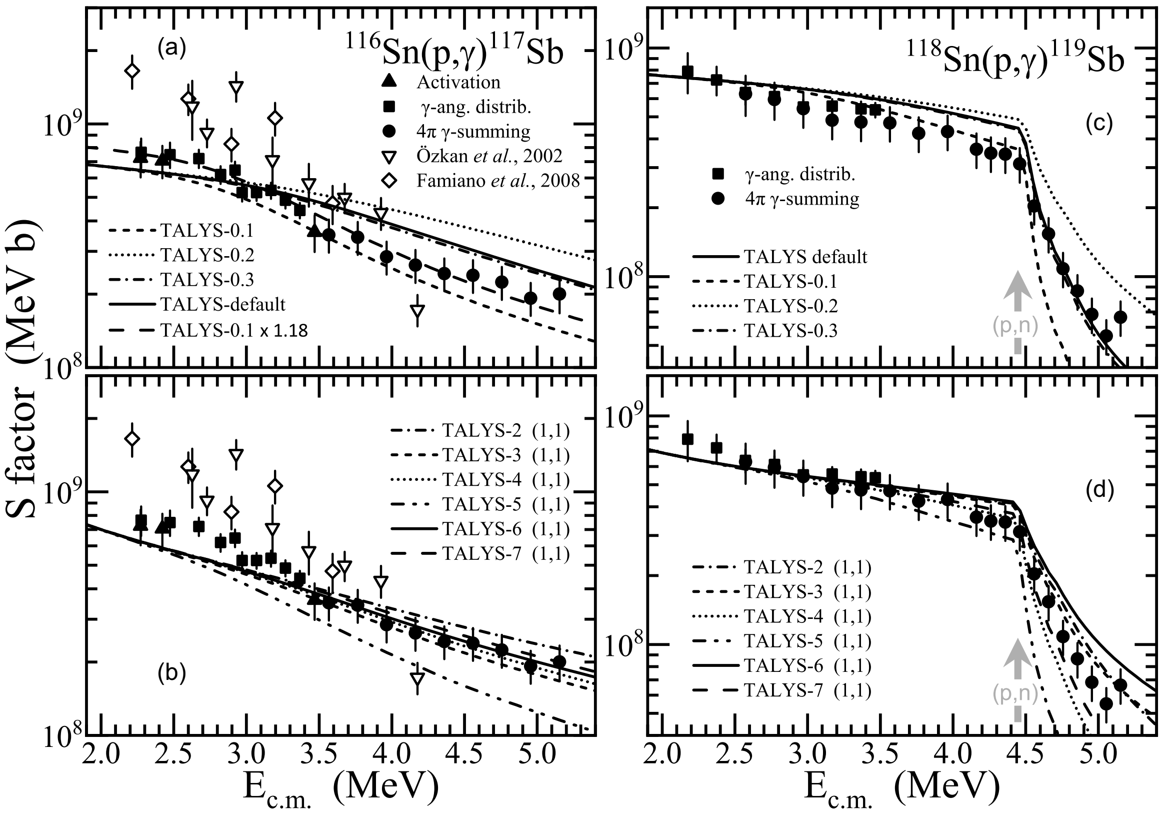

FIG. 13. Panels (a) and (b): Comparison of the screening-corrected S factors (black symbols) obtained in the present work for the $^{116}\mathrm{Sn}(p,\gamma)^{117}\mathrm{Sb}$ reaction with the corresponding TALYS calculations (curves) using the model combinations listed in Table VII and specified in the legends using different types of curves. In panel (a), the curves correspond to the S factors calculated with combinations of purely phenomenological models. Panel (b) displays the S factors calculated with combinations of semimicroscopic models. The black data symbols and the pairs of values given in parentheses are explained in the text. Panels (c) and (d): Same as in panels (a) and (b), but for the $^{118}\mathrm{Sn}(p,\gamma)^{119}\mathrm{Sb}$ reaction (see text for more details). They gray arrows shown in panels (c) and (d) indicate the energy where the (p,n) channel opens. In the case of the $^{116}\mathrm{Sn}(p,\gamma)^{117}\mathrm{Sb}$ reaction this occurs at is 5.5 MeV.

reproduce the screening-corrected S factors at center-of-mass energies below ≈3.2 MeV. Additionally, TALYS-5 exhibits significant deviations from the experimental data across all energies measured. This deviation is also evident for the $^{118}\mathrm{Sn}(p,\gamma)^{119}\mathrm{Sb}$, as shown in panel (d). Similar deviations of TALYS-5 calculations from experimental data have been observed in several of our previous (p,γ) measurements in other isotopes.

Attempts in the present work to achieve a satisfactory agreement between TALYS-5 calculations and the experimental data by varying λ_V and λ_W, as described below, were not successful. As such, one of the primary findings of this work is that TALYS-5 is not a suitable model combination for HF cross-section calculations of (p,γ) reactions.

The screening-corrected S factors obtained in the present work for the $^{118}\mathrm{Sn}(p,\gamma)^{119}\mathrm{Sb}$ reaction are presented in panels (c) and (d) of Fig. 13. Black squares indicate the S factors derived from γ-angular distribution measurements, while black circles correspond to S factors obtained with the 4π γ-summing method.

In panel (c), the S factors calculated using the combinations of purely phenomenological models listed in Table VII are depicted, while those shown in panel (d) are obtained with combinations of semi-microscopic models, also listed in the same Table VII. Each TALYS curve is identified by a different curve type as indicated by the corresponding legends.

In panel (c) of Fig. 13, TALYS-0.2 fails entirely to reproduce the experimentally derived screening-corrected S factors, consistent with the results for the $^{116}\mathrm{Sn}(p,\gamma)^{117}\mathrm{Sb}$ reaction. The S factors calculated with the TALYS-default and TALYS-0.3 combinations are, again, almost identical within the displayed energy range, differing by less than 4%.

As shown in this panel, TALYS-default and TALYS-0.3 reproduce very well the experimental S factors determined at energies where the (p,n) channel is open. However, they overestimate the S factors below the (p,n) threshold (≈4.477 MeV). In contrast, the S factors calculated with TALYS-0.1 combination are in good agreement with those obtained below the (p,n) threshold but underestimate the S factors derived above the opening of the (p,n) channel.

In contrast to the phenomenological model combinations shown in panel (c) of Fig. 13, the semi-microscopic ones, depicted in panel (d), are, in general, in good agreement with the screening-corrected S factors obtained below the (p,n) threshold. Above this threshold, deviations are observed, but these combinations generally follow the energy dependence indicated by the experimentally obtained S factors. It is worth noting again that TALYS-5 produces the smallest S factors for the ^{118}Sn$(p,\gamma)^{119}$Sb reaction.

B. Local improvement of the JLM/B OMP

1. Present (p,γ) measurements on ^{116}Sn and ^{118}Sn

In our last paper on (p,γ) cross-section measurements on Sr isotopes [22], we presented a detailed analysis procedure aimed at improving the widely used Lane-consistent semimicroscopic JLM/B p-OMP [38,39]. This analysis was primarily motivated by the need to investigate whether the predictive power of JLM/B is comparable to the well-regarded phenomenological KD p-OMP [40], which is almost routinely used in HF calculations.

For our discussion, we recall that the general functional form of the JLM/B OMP is given by

$$U = \lambda_V[V_0 \pm \lambda_{V1}\alpha V_1] + i\lambda_W[W_0 \pm \lambda_{W1}\alpha W_1] + U_{\mathrm{SO}}, \quad (8)$$

where V_0 and W_0 are, respectively, the real and imaginary isoscalar components of the central potential seen by a proton (neutron). Accordingly, V_1 and W_1 are the real and imaginary isovector components of the central potential and U_{SO} is the component of the potential due to spin-orbit interaction. The $\lambda_{V,W}$ and $\lambda_{V1,W1}$ are the energy dependent normalization factors for the real isoscalar, imaginary isoscalar, real isovector, and imaginary isovector components, respectively, which were introduced in [38,39] to adjust the OMP to experimental data.

In the case of the (p,γ) reactions on the stable Sr isotopes [22], we were able to optimize the JLM/B p-OMP by adjusting the isoscalar normalization factors and comparing the resulting TALYSC cross sections with the experimental data. It is worth noting that a similar analysis could, in principle, be conducted for the isovector normalization factors λ_{V1} and λ_{W1}. However, as concluded in [72], varying λ_{V1} and λ_{W1} has a much weaker effect on the cross-section calculations compared to the variation of λ_V and λ_W. Therefore, our analysis was focused exclusively on these isoscalar components. To facilitate this, we adopted the multiplicative factors introduced in [72], i.e.,

$$\lambda'_V(E) = f_V\lambda_V(E) \quad (9)$$

and

$$\lambda'_W(E) = f_W\lambda_W(E). \quad (10)$$

Adjusting the values of f_V and f_W to improve the JLM/B p-OMP is not an arbitrary procedure; as suggested in [33,38,39], f_V and f_W can be varied within the range of 0.5 to 1.5. To facilitate this adjustment in TALYS 1.96, the built-in keywords “lvadjust” and “lwadjust” can be used, respectively.

It is worth noting that while it is possible to identify a pair of f_V and f_W values that yield an overall good agreement between the experimental data and the TALYS calculations, this pair may not necessarily improve the JLM/B p-OMP if the resulting TALYS calculations fail to reproduce the experimental data at energies where the HF calculations depend solely on the p-OMP and are not affected by other nuclear parameters, such as the NLD and γSF.

In the case of the (p,γ) cross-section measurements on stable Sr isotopes [22], we found that at energies below ≈2.2 MeV the HF calculations depend only on the p-OMP (see Fig. 12 of Ref. [22]). Subsequently, the optimization of the JLM/B p-OMP was achieved by adjusting the parameters f_V and f_W and selecting the pair of values that yielded the best agreement between TALYS calculations and experimental cross sections measured at energies below ≈2.2 MeV.

Based on these findings, one can conclude that the lower the proton energies are at which experimental cross sections are available, the more suitable they are for optimizing the JLM/B p-OMP. However, it is important to note that in the present work TALYS calculations at the lowest measured energies are not exclusively dependent on the p-OMP; they also depend on the NLD and the γSF. This dependency is clearly illustrated in Fig. 14 by the shaded areas, as further explained below.

Panels (a) and (b) of Fig. 14 illustrate the screening-corrected experimental cross sections obtained for the ^{116}Sn$(p,\gamma)^{117}$Sb and ^{118}Sn$(p,\gamma)^{119}$Sb reactions, respectively. Here, we use the same symbols as in Fig. 13 to indicate these data, as indicated in the legends.

The screening-corrected S factors obtained from the cross sections displayed in panels (a) and (b) of Fig. 14 are shown in panels (c) and (d). In all four panels, the black solid curves represent S factors calculated using the TALYS-default model combination, which incorporates the SMLO γSF model [62,63]. It is worth noting that this TALYS-default combination differs from the default combination used in our previous publications, where calculations were conducted with TALYS 1.95 and the γSF model of Kopecky and Uhl [59,60], instead of the SMLO model.

The shaded areas, as depicted in Fig. 14, indicate the range of cross-section values calculated using all 576 possible combinations of the phenomenological KD OMP [40], along with all available α-OMPs, NLD, and γSF models available in TALYS (see Table VI).

As seen in panels (a) and, notably, in (c) of Fig. 14, the shaded areas vanish for the ^{116}Sn$(p,\gamma)^{117}$Sb reaction at energies below ≈2.2 MeV, which corresponds to the energy range where experimental cross sections are not available. In the case of ^{118}Sn$(p,\gamma)^{119}$Sb, this occurs at $E_{\mathrm{c.m.}} \lessapprox 2.4$ MeV, where, as shown in panel (d), only one cross section was measured. The disappearance of these shaded areas indicates that below these energies the HF calculations do not depend on the NLDs and the γSFs; instead, they solely depend on the choice of the p-OMP.

In the above analysis, we considered not only the (p,γ) channel but also its competing ones, including (p,n), (p,p'), and (p,α). However, it is important to note that, at the energies considered, these competing channels are neither open nor as prominent as the (p,γ). Specifically, the (p,n) thershold of the ^{116}Sn$(p,\gamma)^{117}$Sb reaction is at 5.534 MeV, while for the case of ^{118}Sn$(p,\gamma)^{119}$Sb it is at 4.477 MeV. Furthermore, as indicated by the dotted curves, the corresponding (p,p') results calculated with the TALYS-default model combination are nearly two orders of magnitude weaker. Finally, the (p,α)

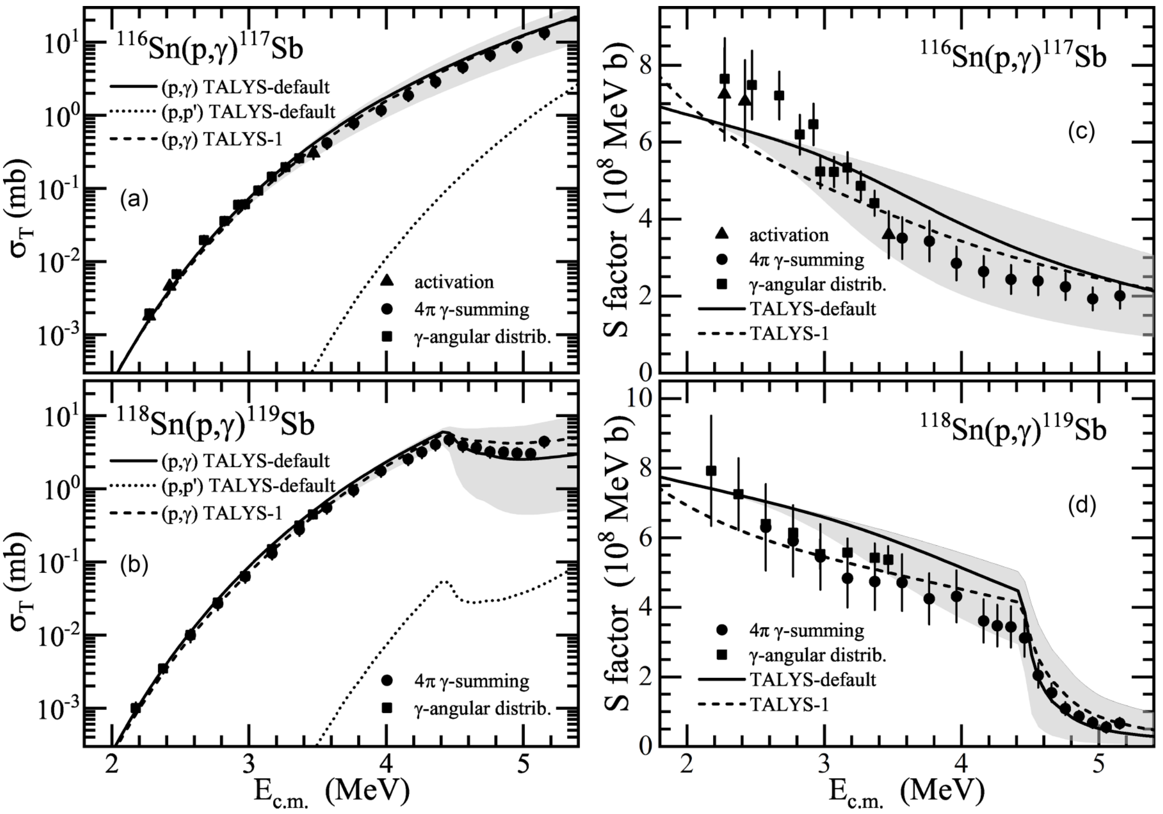

FIG. 14. Panels (a) and (b): Screening-corrected experimental cross sections (black symbols) determined in the present work for the ^{116}Sn$(p,\gamma)^{117}$Sb and ^{118}Sn$(p,\gamma)^{119}$Sb reactions, respectively. The corresponding TALYS-default and TALYS-1 calculations are plotted using different curve types as indicated in the legends. The data symbols and the shaded areas are explained in the text. Panels (c) and (d): Same as in panels (a) and (b) but for the corresponding *S* factors.

reaction channel is so negligible that it is not displayed in Fig. 14.

Panels (c) and (d) of Fig. 14 depict the TALYS-default and TALYS-1 calculations with solid and dashed curves, respectively. Both curves show deviations from the experimental data. For the ^{116}Sn$(p,\gamma)^{117}$Sb reaction, the average deviation of both curves from the data is 17%. For the ^{118}Sn$(p,\gamma)^{119}$Sb reaction, TALYS-1 deviates by 16%, while TALYS-default deviates by 23%. Nonetheless, these two curves indicate the very different energy dependence between the HF calculations performed with the two OMPs, KD and JLM/B.

Based on Fig. 14, one can conclude that the lack of experimental data at energies, where the HF calculations depend entirely on the *p*-OMP, challenges the JLM/B OMP optimization procedure because the methodology used in our recent (p,γ) cross-section measurements on the Sr isotopes [22] cannot be applied in this case. Similar examples of (p,γ) cross section measurements in which experimental data are lacking at energies where the HF calculations depend entirely on the *p*-OMP can be found in, e.g., [20,73–76].

Nevertheless, in the present work, we made an effort to "locally" improve the JLM/B OMP using the available cross-section data. For this purpose, we used the semi-microscopic model combinations listed in Table VII, except for TALYS-5, in order to investigate which f_V and f_W values of the JLM/B *p*-OMP reproduce best the experimental data for all energies measured.

Before presenting the results of this analysis it is essential to explore how the variation of the f_V and f_W values affect the TALYS calculations when using the JLM/B OMP. For this purpose, we have chosen the TALYS-3 model combination and the ^{116}Sn$(p,\gamma)^{117}$Sb reaction as an illustrative example.

The results of this analysis are demonstrated in Fig. 15, were the relevant calculations are plotted with solid, dashed or dashed-dotted curves. The corresponding pairs of f_V and f_W values are indicated in parentheses within the legends. The symbols used to denote the experimental data are the same as in Fig. 13.

In panel (a) of Fig. 15, the displayed TALYS curves result from varying f_V between 0.70 and 1.05, while keeping f_W at its default value (=1), which is used in "standard" TALYS calculations. In panel (b), f_W is varied between 0.8 and 1.5, with no change in the default value of f_V (=1).

Based on panel (a) of Fig. 15, it can be concluded that even a minor variation in f_V can result in significant deviations in the *S* factors, particularly at energies below ≈ 3 MeV. It is worth noting that the observed pattern of TALYS-3 curves in panel (a) may not necessarily apply to other (p,γ) reactions, particularly those involving target nuclei in very different mass regions. However, it highlights the energy range where the variation of f_V has the most pronounced impact.

In our analysis, we observed that an increase in f_V above its default value (=1) can result in smaller *S* factors at energies

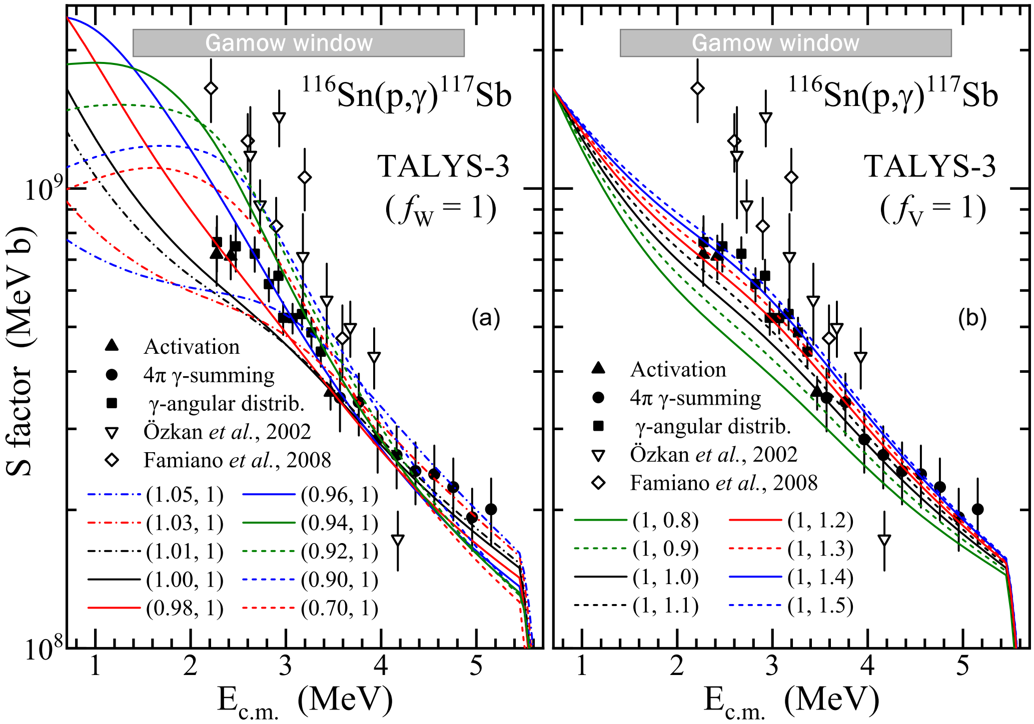

FIG. 15. Comparison of the screening-corrected S factors obtained in the present work (black symbols) and from Refs. [70,71] (open symbols) for the ^{116}Sn(p, γ)^{117}Sb reaction with the S factors calculated with TALYS-3 (solid, dashed, and dashed-dotted curves). The different pairs of (f_V, f_W) values used in these calculations are given in parentheses and are distinguished by different colors, as specified in the legends. The TALYS-3 curves along with the black and gray data symbols are explained in the text. The gray bar shown in both panels indicate the relevant Gamow window for (p, γ) reactions on the Sr isotopes and corresponds to a stellar temperature region (1.8–3.3) × 10^9 K.

down to 1 MeV when compared to the "standard" calculations, where $f_V = f_W = 1$. This can be seen when comparing the blue dashed-dotted curve obtained with $f_V = 1.05$ with the black one obtained with $f_V = 1.00$.

On the other hand, decreasing f_V below its default value yields higher S factors. This is shown by, e.g., the green solid curve in panel (a) of Fig. 15, corresponding to $f_V = 0.94$, which shows higher values compared to the black solid curve. However, this trend holds only up to a certain "critical value," which in this case is $f_V = 0.94$. Further reduction below this critical value results in decreasing S factors. This can be seen when comparing the green solid curve with the dashed curves corresponding to f_V values of 0.92, 0.90, or 0.70.

Panel (b) of Fig. 15 demonstrates how the variation of the value of f_W in TALYS-3 calculations leads to different S factors. In this panel, the various TALYS-3 curves correspond to f_W values ranging between 0.8 and 1.5, while $f_V = 1$ in all cases. A distinct pattern emerges, where $f_W > 1$ result in higher S factors, and vice versa. Additionally, the S factors obtained with different f_W values exhibit less deviation from each other compared to the case of f_V variation. Notably, the energy region affected by changing f_W is slightly higher than that impacted by variations in f_V.

With an understanding of how TALYS calculations depend on f_V and f_W, we proceeded with varying their values incrementally, with a step = 0.01. The results of this analysis are shown in Fig. 16.

For the case of the ^{116}Sn(p, γ)^{117}Sb reaction, shown in panels (a) and (b) of Fig. 16, we found that the pair $(f_V, f_W) = (0.97, 0.95)$ reproduces best our screening-corrected S factors using the semimicroscopic models of Table VII, with the exception of TALYS-3, for which a different pair, (1.00, 1.40), appears to do so. It is worth noting that in [72], Vagena *et al.* proposed the pair $(f_V, f_W) = (1.00, 1.50)$ for (p, γ) reactions on Sn isotopes. This pair is the recommended one for optimizing the global character of the JLM/B OMP.

For the ^{118}Sn(p, γ)^{119}Sb reaction, as demonstrated in panels (c) and (d) of Fig. 16, we found that the pair $(f_V, f_W) = (0.97, 0.90)$ yields the best agreement between the screening-corrected S factors obtained from our experiments and the calculations performed with TALYS-2, TALYS-3, or TALYS-6.

In the case of TALYS-4 and TALYS-7, this pair provides equally good results, but only for energies below the opening of the (p, n) channel, which occurs at ≈4.48 MeV. As discussed below, the deviations observed above 4.48 MeV are most likely attributed to the NLD model used in the corresponding calculations.

Finally, to illustrate the sensitivity of our experimental data in deriving the best f_V and f_W values, we plot in panel (c) of Fig. 16, a shaded area that indicates the range of minimum and maximum S factors resulting from calculations with TALYS-2, using the values (0.96, 0.85) and (0.98, 0.95) for the pair (f_V, f_W), respectively. As depicted in this panel, the shaded area becomes more pronounced at energies below ≈2.5 MeV.

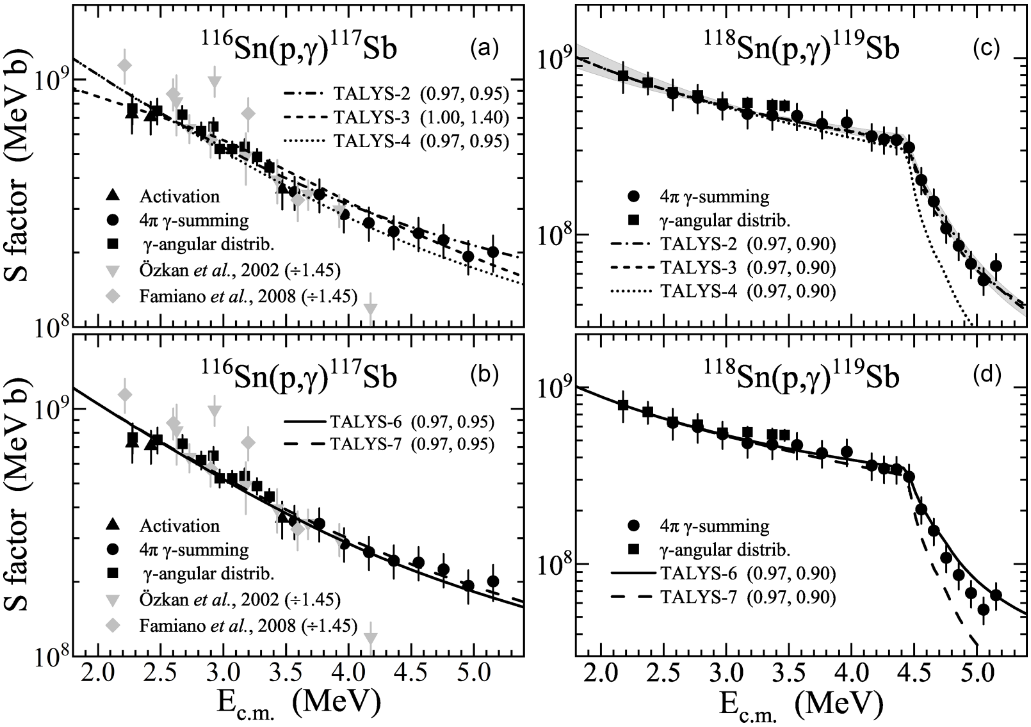

FIG. 16. Panels (a) and (b): Comparison of the S factors calculated with TALYS (curves) using combinations of semimicroscopic models with the screening-corrected S factors obtained in the present work (black symbols) for the $^{116}\mathrm{Sn}(p,\gamma)^{117}\mathrm{Sb}$ reaction. The black and gray data symbols are explained in the text. The model combinations are specified in the legends and the corresponding calculations are shown with different types of curves. The values of the (f_V, f_W) pairs used in the calculations are indicated in parentheses. Panels (c) and (d): Same as in panels (a) and (b) but for $^{118}\mathrm{Sn}(p,\gamma)^{119}\mathrm{Sb}$.

Considering these findings, we can conclude that the experimental data from both investigated reactions are well-reproduced by both the TALYS-2 and TALYS-6 model combinations when using $f_V = 0.97(1)$ and $f_W = 0.90(5)$.

2. (p,γ) measurements on other Sn isotopes.

In addition to the (p,γ) cross-section measurements in ^{116}Sn reported in [70], Famiano *et al.* investigated the $^{114}\mathrm{Sn}(p,\gamma)^{115}\mathrm{Sb}$ reaction using the activation technique and the measured cross sections are also provided in [70]. Furthermore, Chloupek *et al.* reported in [77] S factors for the $^{112}\mathrm{Sn}(p,\gamma)^{113}\mathrm{Sb}$ and $^{119}\mathrm{Sn}(p,\gamma)^{120}\mathrm{Sb}$ reactions, which were also obtained from cross sections measured with the activation technique.

In our effort to locally improve the JLM/B OMP, as described above, we also considered the data reported in Refs. [70,77] for these three reactions. For this purpose, we corrected the cross sections reported in [70] for electron screening and subsequently used them to derive the screening-corrected S factors for the $^{114}\mathrm{Sn}(p,\gamma)^{115}\mathrm{Sb}$ reaction.

For the $^{112}\mathrm{Sn}(p,\gamma)^{113}\mathrm{Sb}$ reaction, we corrected the S factors reported in [77] for electron screening. The same corrections applied for the $^{119}\mathrm{Sn}(p,\gamma)^{120}\mathrm{Sb}$ reaction, using the S factors given in the EXFOR database [78], which contains the S factors reported in [77] after being corrected by its authors.

In the case of $^{112}\mathrm{Sn}(p,\gamma)^{113}\mathrm{Sb}$, as shown in panel (a) of Fig. 17, the "standard" TALYS-6 combination reproduces the screening-corrected S factors very well. The TALYS-6 calculations with $(f_V, f_W) = (0.98, 1)$ reproduce the S factors equally good. It is worth noting that, in our analysis we found that, any other variations in f_V or f_W did not result in a better agreement with the data. For completeness, the calculations with the TALYS-2, TALYS-3, and TALYS-default combinations are also included in all panels of Fig. 17.

The S factors of the $^{114}\mathrm{Sn}(p,\gamma)^{115}\mathrm{Sb}$ reaction are best reproduced by TALYS-6 using $(f_V, f_W) = (0.98, 1)$. These calculations reproduce all data points, including the one obtained at the lowest proton energy measured. This is not the case for any calculations performed with other TALYS combinations. However, the "standard" TALYS-3, TALYS-6, and TALYS-default calculations result also in an overall good agreement with the experimental data because they reproduce all the other data points. Nevertheless, panel (b) of Fig. 17 highlights the need for additional experimental data at low energies below 2.4 MeV in order to improve the "global" character of the JLM/B OMP.

In the case of the $^{119}\mathrm{Sn}(p,\gamma)^{120}\mathrm{Sb}$ reaction, none of the "standard" semimicroscopic combinations of TALYS reproduces the screening-corrected S factors obtained from the work of Chloupek *et al.* [77,78]. This also applies to TALYS-default. Furthermore, the energy dependence of the Chloupek data differs substantially from that indicated by any TALYS

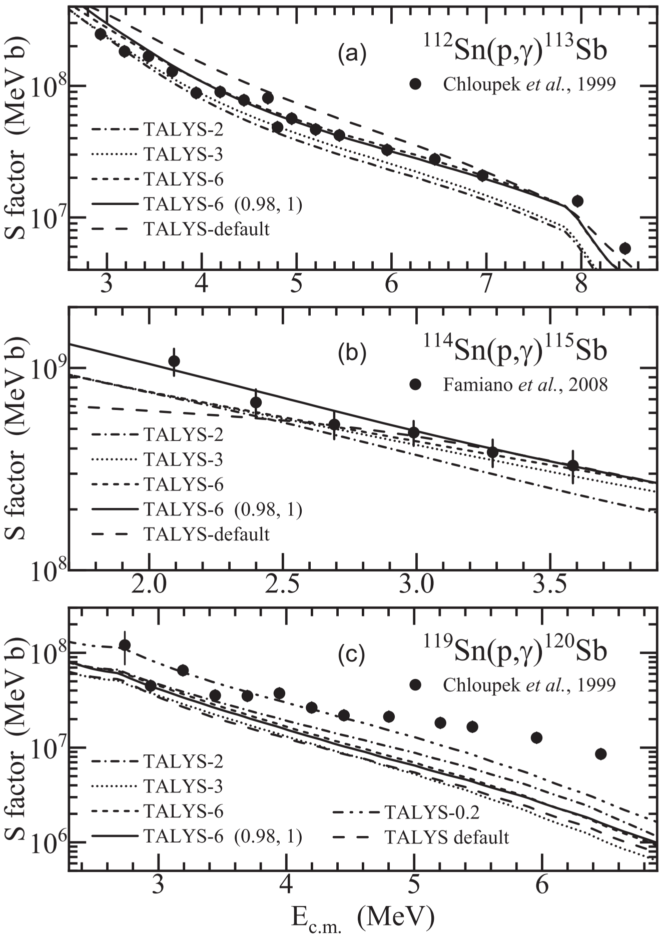

FIG. 17. Comparison of the screening-corrected S factors obtained from [70,77,78] for the (p, γ) reactions on ^{112}Sn, ^{114}Sn and ^{119}Sn with the corresponding TALYS calculations (see text for details).

calculation, regardless of the model combination or the f_V and f_W values used.

In our view, it would be beneficial to repeat the cross-section measurements of this reaction using an in-beam technique to unravel the underlying reasons for the significant disagreement between statistical model calculations and experimental S factors.

C. Nuclear level densities and gamma-ray strength functions

As concluded in Sec. IV B 1, the experimental screening-corrected S factors obtained in the present work for the ^{116}Sn(p, γ)^{117}Sb and ^{118}Sn(p, γ)^{119}Sb reactions, are very well reproduced by both TALYS-2 and TALYS-6 model combinations when using the pairs $(f_V, f_W) = (0.97, 0.95)$ and $(f_V, f_W) = (0.97, 0.90)$, respectively. Both combinations make use of the JLM/B OMP but employ different models for NLDs and γSFs (as detailed in Table VII).

The different NLD models used by TALYS-2 and TALYS-6 could be further validated by comparing the corresponding predictions for other nuclear quantities, such as the s-wave resonance spacings D_0 measured for the produced compound nuclei ^{117}Sb and ^{119}Sb. Additionally, the cumulative number $N_{\rm cum}$ of their excited levels with energies below or around their neutron separation energies could be compared.

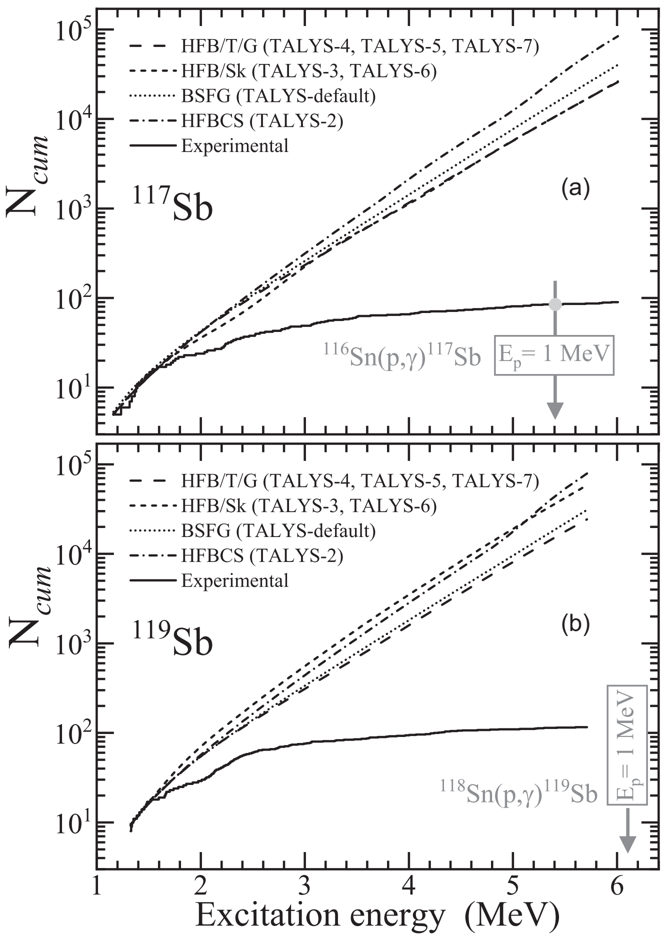

FIG. 18. Panel (a): Comparison of the cumulative number ($N_{\rm cum}$) of low-lying levels observed in ^{117}Sb with the corresponding predictions of the different NLD models used in our TALYS 1.96 calculations. Panel (b): Same as in panel (a) but for the ^{119}Sb nucleus (see also text).

Likewise, the predictions of the various γSF models used by TALYS-2 and TALYS-6 could be directly compared with experimentally determined γSFs. Moreover, one could also compare the total radiative widths Γ_γ predicted by TALYS-2 and TALYS-6 with the corresponding experimental data. However, it is important to keep in mind that Γ_γ is an integral over the γSF and NLD, and therefore it depends on both the γSF and the NLD models used to calculate them.

Unfortunately, there are no experimental data on s-wave resonance spacings D_0, radiative widths Γ_γ, and γSF for the ^{117}Sb and ^{119}Sb nuclei. Consequently, in panels (a) and (b) of Fig. 18, we compare the experimental cumulative number $N_{\rm cum}$ of ^{117}Sb and ^{119}Sb, respectively, with the corresponding $N_{\rm cum}$ calculated with the NLD models listed in Table VII. The NLD model predictions are shown by curves with different colors as indicated in the legends. The associated TALYS combinations are given in parenthesis for each case.

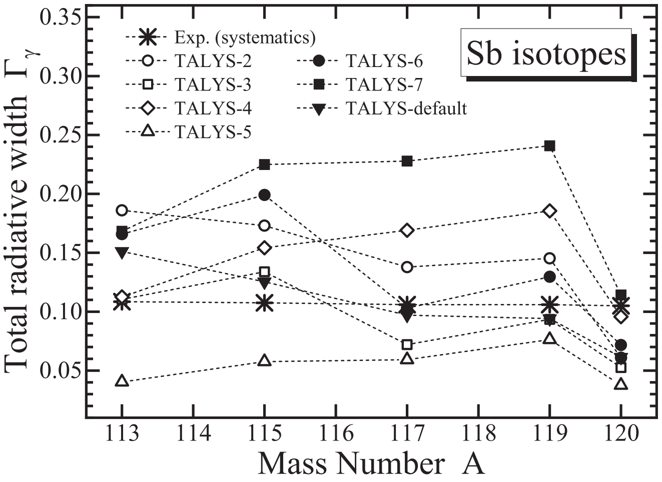

FIG. 19. Comparison of the total radiative widths Γ_γ of the ^{113,115,117,119,120}Sb isotopes calculated with the purely phenomenological TALYS-default model combination and the semimicroscopic combinations listed in Table VII with systematics published in [79].

As can be seen in both panels of Fig. 18, all the NLD models listed in Table VII reproduce the low-energy part of the available phase space in the ^{117}Sb and ^{119}Sb compound nuclei quite well. It's worth noting, however, that the experimental cumulative numbers in Fig. 18 refer to excited levels that are populated using very low-energy proton beams. In the case of, e.g., the ^{117}Sb nucleus, the vertical gray arrow pointing to a level energy of 5.394 MeV indicates the expected $N_{\rm cum}$ when the energy E_p of the bombarding protons is 1 MeV.

Unfortunately, there are no experimental cumulative numbers available for the energy region covered by the present measurements, where excited levels with energies up to ≈10 MeV are populated. Additionally, due to lack of experimental data on D_0 we cannot provide constraints or meaningful comparisons of NLDs at higher excitation energies near the neutron separation energies S_n of ^{117}Sb ($S_n = 9.889$ MeV) and ^{119}Sb ($S_n = 9.549$ MeV), which are more relevant to the compound nucleus reactions at the energies studied in the present work.

Due to a shortage in measured average radiative widths Γ_γ, Fig. 19 shows a comparison of the calculated average radiative widths with systematics [79]. According to this figure, the combinations of TALYS-6 and TALYS-default exhibit the best agreement with the systematics for the compound nucleus ^{117}Sb, followed by TALYS-2 and TALYS-3, which deviate from the systematics by less than 30%. In the case of ^{119}Sb, TALYS-3 and TALYS-default reproduce the systematics most accurately, followed by TALYS-6 and TALYS-2.

To gain an overall understanding of the predictive power of the different TALYS combinations used in this work, the corresponding absolute deviations from the systematics could be used as a criterion. These deviations are smallest for the TALYS-3 and TALYS-default combinations, while TALYS-6 and TALYS-4 exhibit slightly larger deviations. This pattern, however, is not fully in line with the conclusions drawn from Fig. 13.

In order to test the recommendation by Koning *et al.* [33] regarding the Skyrme-HFB NLD model [54,55] and the recently developed γSF models, HFB/T/QRPA/G [68,69] and SMLO [62,63], we compared the screening-corrected S factors obtained in the present work and from Refs. [70,71] for the ^{116}Sn$(p,\gamma)^{117}$Sb and ^{118}Sn$(p,\gamma)^{119}$Sb with those calculated by consistently using the JLM/B p-OMP and the αOMP/III α-OMP but different NLD and γSF models.

In panels (a) and (c) of Fig. 20, the S factors calculated with the Skyrme-HFB NLD model [54,55] for the ^{116}Sn$(p,\gamma)^{117}$Sb and ^{118}Sn$(p,\gamma)^{119}$Sb, respectively, are indicated by the dashed curve. The S factors calculated with the other NLD models, namely CTFG, HFBCS, and HFB/T/G, are plotted as solid, dashed-dotted, and dotted curves, respectively. Our screening-corrected S factors are shown as black symbols, whereas the data obtained from [70,71], after being downscaled by a factor of 1.45, as previously discussed, are depicted by the gray rhombs and gray triangles, respectively.

As indicated in the relevant framed legends, all these calculations were performed using the HFB/T/QRPA/G γSFs, the semimicroscopic α-OMP denoted with αOMP/III in Table VI, and the JLM/B OMP with the pairs $(f_V, f_W) =$ $(0.97, 0.95)$ and $(0.97, 0.90)$, which have been shown to best reproduce the experimental data of these reactions. The only variable being changed in these calculations is the NLD model, and each one is specified in the legends using different curve types.

According to panel (a), the calculations exhibit varying degrees of success in reproducing the data, with some models (CTFG, HFBCS) being less successful. Overall, however, the experimental data points are very well reproduced by the TALYS calculations, regardless of the NLD model used.

This observation is true for panel (c) as well, with the exception of the HFB/T/G NLD model, namely the temperature dependent NLDs obtained from a combinatorial method using nuclear structure properties determined with a HFB model and the D1M Gogny force [56]. Based on the above, we also can conclude that the Skyrme-HFB NLD model [54,55] is indeed a robust NLD model and due to its semimicroscopic character, a very good choice for reliable HF calculations.

In panels (b) and (d) of Fig. 20, we compare the same data, plotted in panels (a) and (c), with the S factors calculated using all the γSF listed in Table VI except of the RMF/T. This comparison aims at validating the recommendation of Koning *et al.* [33] concerning the γSF models, and especially to check whether the predictive power of SMLO compares equally well with that of HFB/T/QRPA/G. It is worth recalling again that these two models are the only ones describing consistently the γSF for both $E1$ and $M1$ γ transitions.

For both reactions investigated, we found that the curves corresponding to HFB/T/QRPA/G and SMLO are identical; the long-dashed curve corresponding to HFB/T/QRPA/G model and that corresponding to SMLO cannot be distinguished in panels (c) and (d) from each other. As in the case of the comparison of NLDs shown in panels (a) and (c), the experimental data points are well reproduced by the TALYS calculations, regardless of the γSF model employed.

An interesting conclusion coming out from the comparison of the TALYS-default curves, shown in panels (a) and (c) of

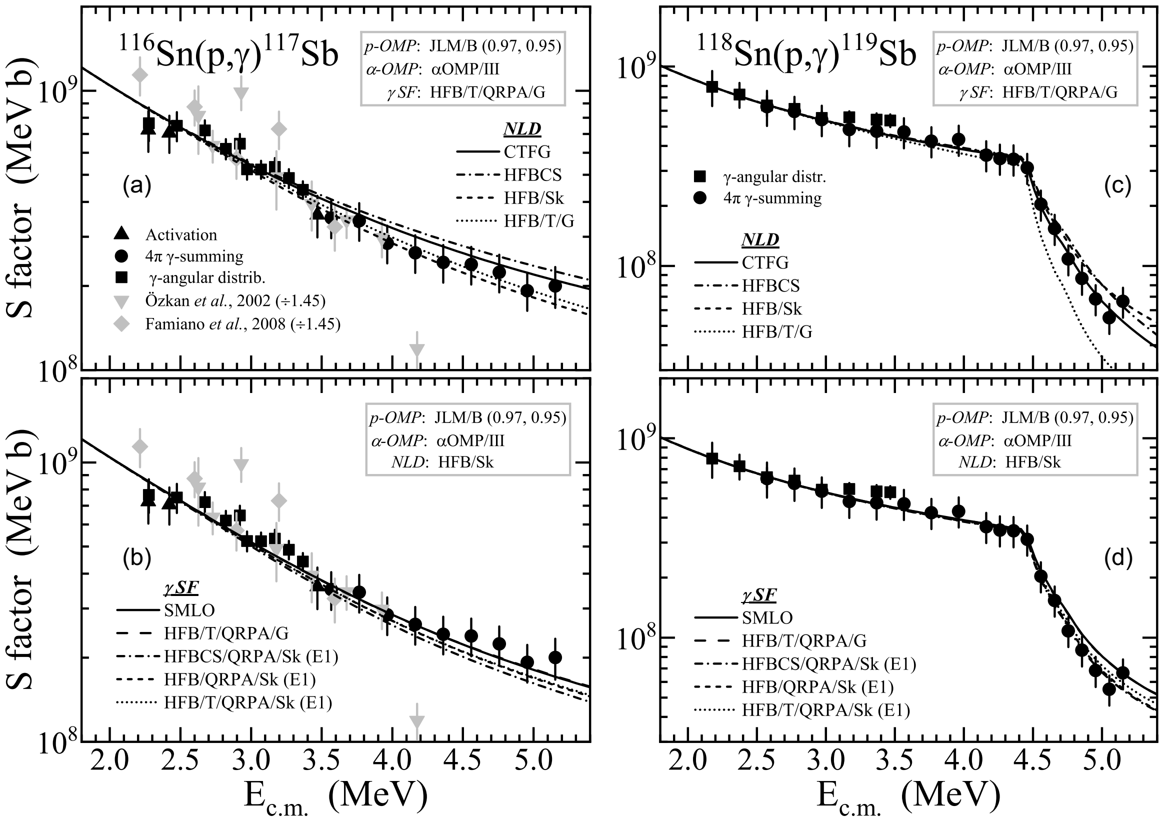

FIG. 20. Panel (a): Screening-corrected S factors obtained in the present work (black symbols) for the ^{116}Sn$(p,\gamma)^{117}$Sb reaction (black symbols) and the S factors calculated with TALYS (curves) using different NLD models combined with the OMPs and γSFs indicated in the framed legend. All models are described in Table VI. The black and gray data symbols are explained in the text. Panel (b): Same as in panel (a) but for TALYS calculations using different γSF model with the OMPs and NLDs specified in the framed legend of panel (b). Panels (c) and (d): Same as in panels (a) and (b), respectively, but for the ^{116}Sn$(p,\gamma)^{117}$Sb reaction (see also text).

Fig. 13, with the solid ones plotted in the same panels of Fig. 20, is that the phenomenological CTFG NLD model reproduces the data very well if combined with the properly improved semimicroscopic JLM/B OMP and the semimicroscopic HFB/T/QRPA/G γSF. Indirectly, this implies that the failure of TALYS-default to reproduce the experimental data, as illustrated in Figs. 13 and 14, is primarly due to the KD OMP rather than to SMLO γSF model. These conclusion needs of course to be tested in other cases of (p,γ) reactions.

D. Reaction rates

The modeling of the p process relies on stellar reaction rates to calculate the abundances of the p nuclei. These reaction rates are provided by well-established and properly updated libraries such as BRUSLIB [80] and REACLIB [81]. They both provide stellar rates for nearly all proton capture reactions.

BRUSLIB rates are calculated with TALYS 1.96 using the phenomenological nucleon-nucleus OMP of Koning and Delaroche [40], the global semi-microscopic α-particle–nucleus OMP developed by Demetriou, Grama, and Goriely [47], the Skyrme-HFB NLD model [54,55] and the γSFs for $E1$ as well as $M1$ transitions from temperature-dependent HFB plus QRPA calculations basen on the D1M Gogny force (HFB/T/QRPA/G) [33,68,69].

REACLIB reaction rates are calculated with the NON-SMOKER$^{\rm WEB}$ HF code [36] and its upgraded version, SMARAGD [37]. Hereby, the default model combination applied to calculate stellar rates uses the microscopic OMP of Jeukenne *et al.* [82,83], the phenomenological model of McFadden and Satchler [43] for the α-particle–nucleus OMP and the phenomenological γSF and NLD models from Refs. [84] and [85], respectively.

In panel (a) of Fig. 21, we plot the ratios R of the total stellar reaction rates given in the REACLIB [81] and BRUSLIB [80] databases over the corresponding rates obtained in this work using the TALYS-6 semimicroscopic model combination with $(f_V, f_W) = (0.97, 0.95)$. The choice of TALYS-6 for this comparison was guided by the aforementioned recommendation of Koning *et al.* [33] regarding the semi-microscopic NLD and γSF models, which are used by TALYS-6.

In panel (b) of Fig. 21 we plot the corresponding ratios for the ^{116}Sn$(p,\gamma)^{117}$Sb reaction. In this case, the rates for TALYS-6, TALYS-2, and TALYS-3 were obtained with $(f_V, f_W) = (0.97, 0.90)$ for all three model combinations.

In both cases shown in Fig. 21, the REACLIB stellar rates exhibit significant deviations from the corresponding TALYS-6 ones. In the temperature range relevant to the p process,

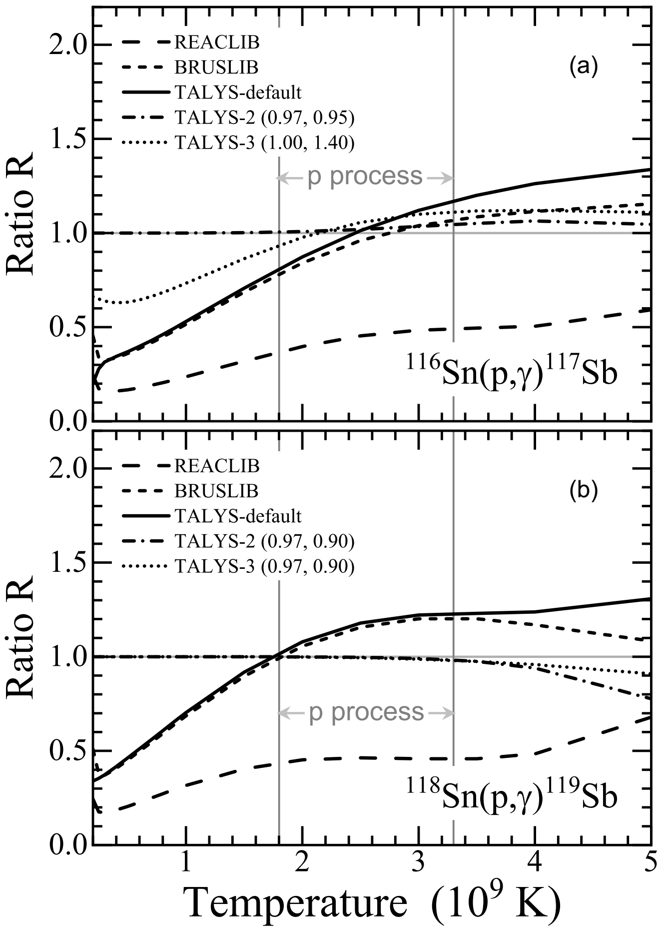

FIG. 21. Ratios R of the stellar reaction rates of the REACLIB [81] and BRUSLIB [80] databases over those obtained for the two (p,γ) reactions investigated in the present work using the semimicroscopic model combination TALYS-6. The respective ratios for the TALYS-default, TALYS-2, and TALYS-3 model combinations are also plotted with curve types, as indicated in the legends (see also text for details).

as indicated by the two vertical gray lines, the REACLIB rates are by a factor 2 smaller than the TALYS-6 rates. In the same range, for the $^{116}\mathrm{Sn}(p,\gamma)^{117}\mathrm{Sb}$ reaction, the TALYS-2 and TALYS-3 rates obtained with the (f_V, f_W) pairs mentioned above do not deviate more than 10% from the corresponding TALYS-6 rates. Additionally, for the $^{118}\mathrm{Sn}(p,\gamma)^{119}\mathrm{Sb}$ reaction, they are almost equal with those derived with TALYS-6 and $(f_V, f_W) = (0.97, 0.90)$.

Based on the ratios shown in Fig. 21, it can be observed that the BRUSLIB rates do not significantly differ from those obtained with the phenomenological TALYS-default combination. Moreover, in the temperature range relevant to the p process, they deviate by no more than 20% from those obtained with the TALYS-6 combination and the (f_V, f_W) pairs mentioned above.

V. SUMMARY AND CONCLUSIONS

In the present work, we determined both total and partial cross sections for the $^{116}\mathrm{Sn}(p,\gamma)^{117}\mathrm{Sb}$ and $^{118}\mathrm{Sn}(p,\gamma)^{119}\mathrm{Sb}$ reactions at energies ranging from 2.2 to 5.2 MeV. These energies cover almost entirely the Gamow window relevant to p-process nucleosynthesis.

Hauser-Feshbach calculations were also performed using the version 1.96 of the TALYS code [33]. For this purpose different combinations of phenomenological or semimicroscopic models describing the proton-nucleus optical model potential (p-OMP), the alpha-particle–nucleus optical model potential (α-OMP), the nuclear level density (NLD), and the γ-ray strength function (γSF) were employed.

Significant deviations were observed between the screening-corrected S factors derived from the measured cross sections and the corresponding TALYS calculations performed with the most widely used phenomenological models listed in Table VII. The most pronounced discrepancies were observed when employing the Brink-Axel γSF for $E1$ γ transitions [57,58]. Large deviations resulting from the use of the Brink-Axel γSF were also observed in many other (p,γ) reactions previously investigated by our group. We can therefore conclude that the γSF described by the Brink-Axel standard Lorentzian is unsuitable for HF calculations, at least for (p,γ) reactions.

Our experimental data were also employed to assess the reliability of the semimicroscopic OMP, NLD, and γSF models, listed in Table VII. Particular effort was put forth to investigate the global character of the semi-microscopic JLM/B p-OMP [38,39], by comparing the experimentally determined screening-corrected S factors with the respective calculations. For this purpose, calculations were performed with the JLM/B p-OMP in which the isoscalar normalization factors λ_V and λ_W for the real and imaginary components were varied so as to best reproduce the experimental data.

Based on the results of this analysis, as depicted in Fig. 16, we can conclude that the experimentally determined screening-corrected S factors of both reactions investigated in the present work are very well reproduced by both the TALYS-2 and TALYS-6 model combinations when λ_V and λ_W are multiplied by the factors $f_V = 0.97(1)$ and $f_W = 0.90(5)$, respectively. These adjustments also apply to the model combination TALYS-3 in the case of the $^{118}\mathrm{Sn}(p,\gamma)^{119}\mathrm{Sb}$ reaction. It is worth noting that both TALYS-6 and TALYS-3 incorporate the Skyrme-HFB NLD model [54,55], abbreviated as HFB/Sk in Table VI, which, as claimed by Koning *et al.* in [33], is the "most robust" NLD model for HF calculations.

Our experimental data for the $^{116}\mathrm{Sn}(p,\gamma)^{117}\mathrm{Sb}$ reaction were also compared with those reported in Refs. [70,71]. The screening-corrected S factors obtained from these works are consistently higher than our results by an overall factor of ≈1.45 and show strong deviations, particularly at energies below ≈ 3 MeV, from the S factors calculated with the TALYS 1.96 code, regardless of the model combinations used.

Using the TALYS-6 model combination along with the previously adjusted λ_V and λ_W values mentioned above, we calculated the stellar reaction rates for both reactions investigated in the present work. These rates were then compared with those provided in the widely-used BRUSLIB [80] and REACLIB [81] databases. In the temperature range relevant to the p process, we found that the REACLIB stellar rates are approximately a factor of 2 smaller than the TALYS-6 rates. In contrast, the BRUSLIB rates exhibit deviations of no more than 20%.

From the comparison of the screening-corrected S factors obtained from our measurements with the corresponding numerous HF calculations performed in the present work, we can additionally draw the following conclusions:

1. The Skyrme-HFB NLD [54,55] undeniably stands out as a "robust" NLD model, as suggested in [33], and is, therefore, recommended for conducting HF calculations, at least for (p,γ) reactions.
2. Despite the limitations inherent to the statistical approach of the HFBCS NLD model [53], which are elaborated in [33], the predictive capability of this model appears to be quite comparable to the Skyrme-HFB NLD [54,55] in many cases (see, e.g., in [22]). Therefore, HF calculations using the HFBCS NLD model [53] should not *a priori* be considered outdated and may remain relevant in various cases.
3. The HFB/T/QRPA/G γSFs, derived from temperature-dependent HFB plus QRPA calculations using the D1M Gogny force [33,68,69] have been proven very successful in reproducing the screening corrected data obtained in the present work when combined with the Skyrme HFB NLDs [54,55] and the JLM/B OMP. The simplified modified Lorentzian (SMLO) proposed in [62,63] was found to be equally successful when combined with the same NLD and OMP models.
4. The semimicroscopic OMP of Bauge *et al.* [38,39], when properly improved, compares equally well in predictive power with the phenomenological OMP of Koning and Delaroche [40]. The improvement can be achieved by measuring cross sections at properly selected low energies, where the HF calculations rely solely on the p-OMP. These data can be then used to properly adjust the energy dependent normalization factors λ_V and λ_W for the real and imaginary components of the JLM/B p-OMP [38,39], as first presented in [72] and "locally" applied in the present work.
5. In the present work, the energies where the HF calculations depend only on the p-OMP were found to be lower than ≈2.2 MeV. A similar example was presented in our last communication [22], where it was shown that the most suitable energies for the purpose of improving the JLM/B OMP [38,39] were lower than ≈1.8 MeV. These findings indicate that the energy region where the HF calculations depend solely on the p-OMP may vary from reaction to reaction, as already shown in [72].
6. For both reactions investigated in the present work, we observed that TALYS-5, which employs the RMF/T γSF model [33,67], significantly underestimates the data. Similar discrepancies were found in many other (p,γ) reactions previously investigated by our group. We can therefore conclude that the RMF/T γSFs are not suitable for HF calculations.

With the extensive experience gained from studying 30 (p,γ) reactions, we can further sum up

1. Any conclusion drawn in the numerous papers published so far by many research groups regarding the degree of success of HF calculations in reproducting (p,γ) cross sections or S factors relevant to the p process, must be cross-validated with experimental data on key nuclear quantities, such as the s-wave resonance spacings D_0, γSFs, and radiative widths Γ_γ for the produced compound nuclei. These data are very crucial for testing the predictions of different NLD and γSF models and subsequently, for identifying the most suitable model combinations for HF calculations. Unfortunately, in the present case, no experimental information is available for these nuclear parameters.
2. With the exception of a few illustrative cases, the overwhelming majority of the experimental (p,γ) cross sections published to date have been determined at proton-beam energies where Hauser-Feshbach calculations rely on all three critical nuclear input parameters: the OMP, NLD, and γSF. Consequently, many of the conclusions presented in these publications could potentially undergo revision if the suggested cross-validation were feasible. This highlights the need for additional experiments aimed at determining the mentioned nuclear parameters, wherever this is experimentally feasible.
3. The two-step cascade technique and the shape method, as proposed by Voinov *et al.* [86] and Wiedeking *et al.* [87], respectively, may offer two alternative approaches to address this need effectively. These approaches would become especially valuable,if the relevant experiments could simultaneously be conducted with cross-section measurements.
4. Cross-section measurements of capture reactions using inverse kinematics may provide important data for mass regions where targets cannot be easily available, as in, e.g., the Kr isotopes. In this direction, recent experimental efforts reported in [88,89] have successfully demonstrated the applicability of this new approach.

Finally, it is worth emphasizing that, despite the relatively long beam times required to determine cross sections through γ-angular distribution measurements and subsequent time-intensive data analysis, the quantity and quality of experimental information obtained through these measurements significantly surpass those achieved by the other two methods discussed in this paper.

Significant reductions in time-consuming beam times could be achieved by applying the differential cross-section integration (DCI) method, that we presented recently in [2]. This method has already demonstrated its successful application in the case of the ^{88}Sr$(p,\gamma)^{89}$Y reaction. While its potential applicability to other cases requires further verification, we anticipate that implementing DCI will lead to a substantial reduction in the beam time required for cross-section measurements, by a factor of at least ≈ 3 when compared to the beam time needed for γ-angular distribution measurements. Importantly, this reduction does not compromise the data quantity and quality mentioned above.

ACKNOWLEDGMENTS

This work was supported by the Hellenic Foundation for Research and Innovation (H.F.R.I.) under the “2nd Call for H.F.R.I. Research Projects to support Faculty Members and Researchers” (Project No. 4650/ARENA).

[1] W. Hauser and H. Feshbach, The inelastic scattering of neutrons, Phys. Rev. **87**, 366 (1952).

[2] S. V. Harissopulos, Cross-section measurements of capture reactions relevant to p-process nucleosynthesis, Eur. Phys. J. Plus **133**, 332 (2018).

[3] M. Arnould and S. Goriely, The p-process of stellar nucleosynthesis: Astrophysics and nuclear physics status, Phys. Rep. **384**, 1 (2003).

[4] T. Rauscher, N. Dauphas, I. Dillmann, C. Fröhlich, Z. Fülöp, and Gy Gyürky, Constraining the astrophysical origin of the p-nuclei through nuclear physics and meteoritic data, Rep. Prog. Phys. **76**, 066201 (2013).

[5] M. Pignatari, K. Göbel, R. Reifarth, and C. Travaglio, The production of proton-rich isotopes beyond iron: The γ-process in stars, Int. J. Mod. Phys. E **25**, 1630003 (2016).

[6] T. Rauscher, N. Nishimura, R. Hirschi, G. Cescutti, A. St. J. Murphy, and A. Heger, Uncertainties in the production of p nuclei in massive stars obtained from Monte Carlo variations, Mon. Not. R. Astron. Soc. **463**, 4153 (2016).

[7] N. Nishimura, T. Rauscher, R. Hirschi, A. St. J. Murphy, G. Cescutti, and C. Travaglio, Uncertainties in the production of p nuclides in thermonuclear supernovae determined by Monte Carlo variations, Mon. Not. R. Astron. Soc. **474**, 3133 (2018).

[8] S. Harissopulos, E. Skreti, P. Tsagari, G. Souliotis, P. Demetriou, T. Paradellis, J. W. Hammer, R. Kunz, C. Angulo, S. Goriely, and T. Rauscher, Cross section measurements of the ^{93}Nb$(p,\gamma)^{94}$Mo reaction at $E_p = 1.4$–4.9 MeV relevant to the nucleosynthetic *p* process, Phys. Rev. C **64**, 055804 (2001).

[9] G. Gyürky, E. Somorjai, Z. Fülöp, S. Harissopulos, P. Demetriou, and T. Rauscher, Proton capture cross section of Sr isotopes and their importance for nucleosynthesis of proton-rich nuclides, Phys. Rev. C **64**, 065803 (2001).

[10] S. Galanopoulos, P. Demetriou, M. Kokkoris, S. Harissopulos, R. Kunz, M. Fey, J. W. Hammer, G. Gyürky, Z. Fülop, E. Somorjai, and S. Goriely, The ^{88}Sr$(p,\gamma)^{89}$Y reaction at astrophysically relevant energies, Phys. Rev. C **67**, 015801 (2003).

[11] G. Gyürky, Z. Fülöp, E. Somorjai, M. Kokkoris, S. Galanopoulos, P. Demetriou, S. Harissopulos, T. Rauscher, and S. Goriely, Proton induced reaction cross section measurements on Se isotopes for the astrophysical *p* process, Phys. Rev. C **68**, 055803 (2003).

[12] P. Tsagari, M. Kokkoris, E. Skreti, A. G. Karydas, S. Harissopulos, T. Paradellis, and P. Demetriou, Cross section measurements of the ^{89}Y$(p,\gamma)^{90}$Zr reaction at energies relevant to *p*-process nucleosynthesis, Phys. Rev. C **70**, 015802 (2004).

[13] S. Harissopulos, A. Lagoyannis, A. Spyrou, Ch. Zarkadas, S. Galanopoulos, G. Perdikakis, H.-W. Becker, C. Rolfs, F. Strieder, R. Kunz, M. Fey, J. W. Hammer, A. Dewald, K.-O. Zell, P. von Brentano, R. Julin, and P. Demetriou, Proton and alpha-particle capture reactions at sub-Coulomb energies relevant to the p process, J. Phys. G: Nucl. Part. Phys. **31**, S1417 (2005).

[14] A. Spyrou, H.-W. Becker, A. Lagoyannis, S. Harissopulos, and C. Rolfs, Cross-section measurements of capture reactions relevant to the *p* process using a 4π gamma-summing method, Phys. Rev. C **76**, 015802 (2007).

[15] A. Spyrou, A. Lagoyannis, P. Demetriou, S. Harissopulos and H.-W. Becker, Cross section measurements of (p,γ) reactions on Pd isotopes relevant to the *p* process, Phys. Rev. C **77**, 065801 (2008).

[16] A. Sauerwein, J. Endres, L. Netterdon, A. Zilges, V. Foteinou, G. Provatas, T. Konstantinopoulos, M. Axiotis, S. F. Ashley, S. Harissopulos, and T. Rauscher, Investigation of the reaction ^{74}Ge$(p,\gamma)^{75}$As using the in-beam method to improve reaction network predictions for *p* nuclei, Phys. Rev. C **86**, 035802 (2012).

[17] S. Harissopulos, A. Spyrou, A. Lagoyannis, M. Axiotis, P. Demetriou, J. W. Hammer, R. Kunz, and H.-W. Becker, Cross section measurements of proton capture reactions relevant to the *p* process: The case of ^{89}Y$(p,\gamma)^{90}$Zr and ^{121,123}Sb$(p,\gamma)^{122,124}$Te, Phys. Rev. C **87**, 025806 (2013).

[18] S. Harissopulos, A. Spyrou, V. Foteinou, M. Axiotis, G. Provatas, and P. Demetriou, Systematic study of proton capture reactions in medium-mass nuclei relevant to the *p* process: The case of ^{103}Rh and ^{113,115}In, Phys. Rev. C **93**, 025804 (2016).

[19] V. Foteinou, S. Harissopulos, M. Axiotis, A. Lagoyannis, G. Provatas, A. Spyrou, G. Perdikakis, Ch. Zarkadas, and P. Demetriou, Cross section measurements of proton capture reactions on Se isotopes relevant to the astrophysical *p* process, Phys. Rev. C **97**, 035806 (2018).

[20] V. Foteinou, M. Axiotis, S. Harissopulos, P. Dimitriou, G. Provatas, A. Lagoyannis, H.-W. Becker, D. Rogalla, A. Zilges, A. Schreckling, and A. Endres, Cross section measurements of proton capture reactions on Mo isotopes relevant to the astrophysical p process, Eur. Phys. J. A **55**, 67 (2019).

[21] S. Harissopulos, E. Vagena, M. Axiotis, A. Spyrou, G. Provatas, A. Lagoyannis, P. Dimitriou, and H. W. Becker, Capture reaction cross-section measurements relevant to *p* process: the case of (α,γ) reactions on ^{63}Cu, ^{72}Ge, ^{118}Sn and the ^{107}Ag$(p,\gamma)^{108}$Cd reaction, EPJ Web Conf. **227**, 01008 (2020).

[22] S. Harissopulos, E. Vagena, P. Dimitriou, M. Axiotis, S. Galanopoulos, V. Foteinou, and A. Lagoyannis, Cross section measurements of proton capture reactions on Sr isotopes for astrophysics applications, Phys. Rev. C **104**, 025804 (2021).

[23] J. F. Ziegler, The Stopping and Range of Ions in Matter: Code SRIM, available online at http://www.srim.org/.

[24] M. Kolbe, B. Beckhoff, M. Krumrey, and G. Ulm, Thickness determination for Cu and Ni nanolayers: Comparison of completely reference-free fundamental parameter-based X-ray fluorescence analysis and X-ray reflectometry, Spectrochim. Acta, Part B **60**, 505 (2005).

[25] *Handbook of Modern Ion Beam Materials Analysis*, 2nd ed., edited by Y. Wang and M. Nastasi (Cambridge University Press, Cambridge, 2010).

[26] IAEA Live Chart of Nuclides, Nuclear Structure and Decay Data based on the Evaluated Nuclear Structure Data File (ENSDF), https://www-nds.iaea.org/livechart/.

[27] F. Raiola, L. Gang, C. Bonomo, G. Gÿurky, M. Aliotta, H. W. Becker, R. Bonetti, C. Broggini, P. Corvisiero, A. D'Onofrio, Z. Fülöp, G. Gervino, L. Gialanella, M. Junker, P. Prati, V. Roca, C. Rolfs, M. Romano, E. Somorjai, F. Strieder, F. Terrasi *et al.*, Enhanced electron screening in d(d,p)t for deuterated metals, Eur. Phys. J. A **19**, 283 (2004).

[28] F. Raiola, B. Burchard1, Z. Fülöp, G. Gÿurky, S. Zeng, J. Cruz, A. Di Leva, B. Limata, M. Fonseca, H. Luis, M. Aliotta, H. W. Becker, C. Broggini, A. D'Onofrio, L. Gialanella, G. Imbriani, A. P. Jesus, M. Junker, J. P. Ribeiro, V. Roca, C. Rolfs, M. Romano, E. Somorjai, F. Strieder *et al.*, Electron screening in d(d,p)t for deuterated metals: Temperature effects, J. Phys. G: Nucl. Part. Phys. **31**, 1141 (2005).

[29] K. Czerski, A. Huke, P. Heide, and G. Ruprecht, Experimental and theoretical screening energies for the ^{2}H(d,p)^{3}H reaction in metallic environments, Eur. Phys. J. A **27**, 83 (2006).

[30] A. Huke, K. Czerski, P. Heide, G. Ruprecht, N. Targosz, and W. Zebrowski, Enhancement of deuteron-fusion reactions in metals and experimental implications, Phys. Rev. C **78**, 015803 (2008).

[31] K. U. Kettner, H. W. Becker, F. Strieder, and C. Rolfs, High-Z electron screening: the cases ^{50}V(p,n)^{50}Cr and ^{176}Lu(p,n)^{176}Hf, J. Phys. G: Nucl. Part. Phys. **32**, 489 (2006).

[32] C. Iliadis, *Nuclear Physics of Stars* (Wiley-VCH, Weinheim, 2007).

[33] A. Koning, S. Hilaire, and S. Goriely, TALYS: modeling of nuclear reactions, Eur. Phys. J. A **59**, 131 (2023).

[34] A. Koning, S. Hilaire, and S. Goriely, TALYS-Related Software and Databases, https://www-nds.iaea.org/talys/.

[35] M. Herman, R. Capote, B. V. Carlson, P. Oblozinsky, M. Sin, A. Trkov, H. Wienke, and V. Zerkin, EMPIRE: Nuclear reaction model code system for data evaluation, Nucl. Data Sheets **108**, 2655 (2007).

[36] T. Rauscher, online code NON-SMOKER$^{\text{WEB}}$ (2008), https://nucastro.org/websmoker.html.

[37] T. Rauscher, code SMARAGD, http://nucastro.org/smaragd.html.

[38] E. Bauge, J. P. Delaroche, and M. Girod, Lane-consistent, semimicroscopic nucleon-nucleus optical model, Phys. Rev. C **63**, 024607 (2001).

[39] E. Bauge, J. P. Delaroche, and M. Girod, Semimicroscopic nucleon-nucleus spherical optical model for nuclei with $A \geqslant 40$ at energies up to 200 MeV, Phys. Rev. C **58**, 1118 (1998).

[40] A. J. Koning and J. P. Delaroche, Local and global nucleon optical models from 1 keV to 200 MeV, Nucl. Phys. A **713**, 231 (2003).

[41] S. Watanabe, High energy scattering of deuterons by complex nuclei, Nucl. Phys. **8**, 484 (1958).

[42] D. G. Madland, Recent results in the development of a global medium-energy nucleon-nucleus optical-model potential, in *Proceedings of the Specialists' Meeting on Preequilibrium Nuclear Reactions, Semmering, Austria, 1988*, edited by B. Strohmaier (OECD, Paris, 1988), p. 103.

[43] L. McFadden and G. R. Satchler, Optical-model analysis of the scattering of 24.7 MeV alpha particles, Nucl. Phys. **84**, 177 (1966).

[44] V. Avrigeanu, M. Avrigeanu, and C. Mănăilescu, Further explorations of the α-particle optical model potential at low energies for the mass range $A \approx 45$–209, Phys. Rev. C **90**, 044612 (2014).

[45] M. Nolte, H. Machner, and J. Bojowald, Global optical potential for α particles with energies above 80 MeV, Phys. Rev. C **36**, 1312 (1987).

[46] V. Avrigeanu, P. E. Hodgson, and M. Avrigeanu, Global optical potentials for emitted alpha particles, Phys. Rev. C **49**, 2136 (1994).

[47] P. Demetriou, C. Grama, and S. Goriely, Improved global α-optical model potentials at low energies, Nucl. Phys. A **707**, 253 (2002).

[48] A. Gilbert and A. G. W. Cameron, A composite nuclear-level density formula with shell corrections, Can. J. Phys. **43**, 1446 (1965).

[49] W. Dilg, W. Schantl, H. Vonach, and M. Uhl, Level density parameters for the back-shifted Fermi gas model in the mass range 40< A < 250, Nucl. Phys. A **217**, 269 (1973).

[50] M. K. Grossjean and H. Feldmeier, Level density of a Fermi gas with pairing interactions, Nucl. Phys. A **444**, 113 (1985).

[51] A. V. Ignatyuk, K. K. Istekov, and G. N. Smirenkin, Role of collective effects in the systematics of nuclear level densities, Yad. Fiz. **29**, 875 (1979) [Sov. J. Nucl. Phys. **29**, 450 (1979)].

[52] A. V. Ignatyuk, J. L. Weil, S. Raman, and S. Kahane, Density of discrete levels in ^{116}Sn, Phys. Rev. C **47**, 1504 (1993).

[53] P. Demetriou and S. Goriely, Microscopic nuclear level densities for practical applications, Nucl. Phys. A **695**, 95 (2001).

[54] S. Goriely, S. Hilaire, and A. J. Koning, Improved microscopic nuclear level densities within the Hartree-Fock-Bogoliubov plus combinatorial method, Phys. Rev. C **78**, 064307 (2008).

[55] S. Hilaire and S. Goriely, Global microscopic nuclear level densities within the HFB plus combinatorial method for practical applications, Nucl. Phys. A **779**, 63 (2006).

[56] S. Hilaire, M. Girod, S. Goriely, and A. J. Koning, Temperature-dependent combinatorial level densities with the D1M Gogny force, Phys. Rev. C **86**, 064317 (2012).

[57] D. M. Brink, Individual particle and collective aspects of the nuclear photoeffect, Nucl. Phys. **4**, 215 (1957).

[58] P. Axel, Electric dipole ground-state transition width strength function and 7-MeV photon interactions, Phys. Rev. **126**, 671 (1962).

[59] J. Kopecky and M. Uhl, Test of gamma-ray strength functions in nuclear reaction model calculations, Phys. Rev. C **41**, 1941 (1990).

[60] J. Kopecky, M. Uhl, and R. E. Chrien, Radiative strength in the compound nucleus ^{157}Gd, Phys. Rev. C **47**, 312 (1993).

[61] S. Goriely, Radiative neutron captures by neutron-rich nuclei and the r-process nucleosynthesis, Phys. Lett. B **436**, 10 (1998).

[62] S. Goriely and V. Plujko, Simple empirical $E1$ and $M1$ strength functions for practical applications, Phys. Rev. C **99**, 014303 (2019).

[63] S. Goriely, P. Dimitriou, M. Wiedeking, T. Belgya, R. Firestone, J. Kopecky, M. Krticka, V. Plujko, R. Schwengner, S. Siem, H. Utsunomiya, S. Hilaire, S. Peru, Y. S. Cho, D. M. Filipescu, N. Iwamoto, T. Kawano, V. Varlamov, and R. Xu, Reference database for photon strength functions, Eur. Phys. J. A **55**, 172 (2019).

[64] V. A. Plujko, O. M. Gorbachenko, R. Capote, and P. Dimitriou, Giant dipole resonance parameters of ground-state

photoabsorption: Experimental values with uncertainties, At. Data Nucl. Data Tables **123-124**, 1 (2018).

[65] S. Goriely and E. Khan, Large-scale QRPA calculation of E1-strength and its impact on the neutron capture cross section, Nucl. Phys. A **706**, 217 (2002).

[66] S. Goriely, E. Khan, and M. Samyn, Microscopic HFB + QRPA predictions of dipole strength for astrophysics applications, Nucl. Phys. A **739**, 331 (2004).

[67] I. Daoutidis and S. Goriely, Large-scale continuum random-phase approximation predictions of dipole strength for astrophysical applications, Phys. Rev. C **86**, 034328 (2012).

[68] S. Goriely, S. Hilaire, S. Péru, and K. Sieja, Gogny+HFB+QRPA dipole strength function and its application to radiative nucleon capture cross section, Phys. Rev. C **98**, 014327 (2018).

[69] M. Martini, S. Péru, S. Hilaire, S. Goriely, and F. Lechaftois, Large-scale deformed quasiparticle random-phase approximation calculations of the γ-ray strength function using the Gogny force, Phys. Rev. C **94**, 014304 (2016).

[70] M. A. Famiano, R. S. Kodikara, B. M. Giacherio, V. G. Subramanian, and A. Kayani, Measurement of the (p,γ) cross sections of ^{46}Ti, ^{64}Zn, ^{114}Sn, and ^{116}Sn at astrophysically relevant energies, Nucl. Phys. A **802**, 26 (2008).

[71] A. N Özkan, St. J. Murphy, R. N. Boyd, A. L. Cole, M. Famiano, R. T. Güray, M. Howard, L. Şahin, J. J. Zach, R. deHaan, J. Görres M. C. Wiescher, M. S. Islam, and T. Rauscher, Cross section measurements of the ^{102}Pd$(p,\gamma)^{103}$Ag, ^{116}Sn$(p,\gamma)^{117}$Sb, and ^{112}Sn$(\alpha,\gamma)^{116}$Te reactions relevant to the astrophysical rp- and γ-processes, Nucl. Phys. A **710**, 469 (2002).

[72] E. Vagena, M. Axiotis, and P. Dimitriou, Systematics of semi-microscopic proton-nucleus optical potential at low energies relevant to nuclear astrophysics, Phys. Rev. C **103**, 045806 (2021).

[73] J. Mayer, S. Goriely, L. Netterdon, S. Péru, P. Scholz, R. Schwengner, and A. Zilges, Partial cross sections of the ^{92}Mo(p,γ) reaction and the γ strength in ^{93}Tc, Phys. Rev. C **93**, 045809 (2016).

[74] A. Khaliel, T. J. Mertzimekis, E.-M. Asimakopoulou, A. Kanellakopoulos, V. Lagaki, A. Psaltis, I. Psyrra, and E. Mavrommatis, First cross-section measurements of the reactions ^{107,109}Ag$(p,\gamma)^{108,110}$Cd at energies relevant to the *p* process, Phys. Rev. C **96**, 035806 (2017).

[75] A. Psaltis, A. Khaliel, E.-M. Assimakopoulou, A. Kanellakopoulos, V. Lagaki, M. Lykiardopoulou, E. Malami, P. Tsavalas, A. Zyriliou, and T. J. Mertzimekis, Cross-section measurements of radiative proton-capture reactions in ^{112}Cd at energies of astrophysical interest, Phys. Rev. C **99**, 065807 (2019).

[76] F. Heim, J. Mayer, M. Müller, P. Scholz, and A. Zilges, Investigating the ^{109}Ag$(p,\gamma)^{110}$Cd reaction and its underlying nuclear physics, Phys. Rev. C **103**, 055803 (2021).

[77] F. R. Chloupek, A. StJ. Murphy, R. N. Boyd, A. L. Cole, J. Görres, R. T. Guray, G. Raimann, J. J. Zach, T. Rauscher, J. V. Schwarzenberg, R. Tischhauser, and M. C. Wiescher, Measurements of proton radiative capture cross sections relevant to the astrophysical rp- and γ-processes, Nucl. Phys. A **652**, 391 (1999).

[78] Experimental Nuclear Reaction Data (EXFOR), https://www-nds.iaea.org/exfor/.

[79] R. Capote, M. Herman, P. Oblozinsky, P. G. Young, S. Goriely, T. Belgya, A. V. Ignatyuk, A. J. Koning, S. Hilaire, V. Plujko, M. Avrigeanu, O. Bersillon, M. B. Chadwick, T. Fukahori, S. Kailas, J. Kopecky, V. M. Maslov, G. Reffo, M. Sin, E. Soukhovitskii *et al.*, RIPL-Reference input parameter library for calculation of nuclear reactions and nuclear data evaluations, Nucl. Data Sheets **110**, 3107 (2009).

[80] Y. Xu, S. Goriely, A. Jorissen, G. L. Chen, and M. Arnould, Databases and tools for nuclear astrophysics applications: BRUSsels Nuclear LIBrary (BRUSLIB), Nuclear Astrophysics Compilation of REactions II (NACRE II) and Nuclear NETwork GENerator (NETGEN), Astron. Astrophys. **549**, A106 (2013).

[81] R. H. Cyburt, A. M. Amthor, R. Ferguson, Z. Meisel, K. Smith, S. Warren, A. Heger, R. D. Hoffman, T. Rauscher, A. Sakharuk, H. Schatz, F. K. Thielemann, and M. Wiescher, The JINA REACLIB database: Its recent updates and impact on type-IX-ray bursts, Astrophys. J. Suppl. Ser. **189**, 240 (2010).

[82] J.-P. Jeukenne, A. Lejeune, and C. Mahaux, Microscopic calculation of the symmetry and coulomb components of the complex optical-model potential, Phys. Rev. C **15**, 10 (1977).

[83] A. Lejeune, Low-energy optical model potential in finite nuclei from Reid's hard core interaction, Phys. Rev. C **21**, 1107 (1980).

[84] J. J. Cowan, F.-K. Thielemann, and J. W. Truran, The R-process and nucleochronology, Phys. Rep. **208**, 267 (1991).

[85] T. Rauscher, F.-K. Thielemann, and K.-L. Kratz, Nuclear level density and the determination of thermonuclear rates for astrophysics, Phys. Rev. C **56**, 1613 (1997).

[86] A. Voinov, S. M. Grimes, C. R. Brune, M. Guttormsen, A. C. Larsen, T. N. Massey, A. Schiller, and S. Siem, γ-strength functions in ^{60}Ni from two-step cascades following proton capture, Phys. Rev. C **81**, 024319 (2010).

[87] M. Wiedeking, M. Guttormsen, A. C. Larsen, F. Zeiser, A. Görgen, S. N. Liddick, D. Mücher, S. Siem, and A. Spyrou, Independent normalization for γ-ray strength functions: The shape method, Phys. Rev. C **104**, 014311 (2021).

[88] A. Palmisano-Kyle, A. Spyrou, P. A. DeYoung, A. Dombos, P. Gastis, O. Olivas-Gomez, C. Harris, S. Liddick, S. M. Lyons, J. Pereira, A. L. Richard, A. Simon, M. K. Smith, A. Tsantiri, and R. Zegers, Constraining the astrophysical p process: Cross section measurement of the ^{84}Kr$(p,\gamma)^{85}$Rb reaction in inverse kinematics, Phys. Rev. C **105**, 065804 (2022).

[89] A. Tsantiri, A. Palmisano-Kyle, A. Spyrou, P. Mohr, H. C. Berg, P. A. DeYoung, A. C. Dombos, P. Gastis, E. C. Good, C. M. Harris, S. N. Liddick, S. M. Lyons, O. Olivas-Gomez, G. Owens-Fryar, J. Pereira, A. L. Richard, A. Simon, M. K. Smith, and R. G. T. Zegers, Cross-section measurement of the ^{82}Kr$(p,\gamma)^{83}$Rb reaction in inverse kinematics, Phys. Rev. C **107**, 035808 (2023).